IEEE Access
Multidisciplinary | Rapid Review | Open Access Journal

Received 31 January 2025, accepted 3 March 2025, date of publication 18 March 2025, date of current version 1 April 2025.

*Digital Object Identifier 10.1109/ACCESS.2025.3552439*

RESEARCH ARTICLE

# Robust and Unified Semi-Supervised Unmixing of Hyperspectral Imaging for Linear and Multilinear Models

**DANIEL ULISES CAMPOS-DELGADO[1], (Senior Member, IEEE), JUAN NICOLÁS MENDOZA-CHAVARRÍA[1], OMAR GUTIERREZ-NAVARRO[2], (Member, IEEE), LAURA QUINTANA-QUINTANA[3], RAQUEL LEON[3], SAMUEL ORTEGA[3,4], HIMAR FABELO[3,5], CARLOS LÓPEZ[6,7], MARYLÈNE LEJEUNE[6,8], AND GUSTAVO M. CALLICO[3], (Senior Member, IEEE)**

[1]Facultad de Ciencias, Universidad Autónoma de San Luis Potosi, San Luis Potosi 78295, Mexico
[2]Biomedical Engineering Department, Universidad Autónoma de Aguascalientes, Aguascalientes 20100, Mexico
[3]Institute for Applied Microelectronics, University of Las Palmas de Gran Canaria, 35001 Las Palmas de Gran Canaria, Spain
[4]Norwegian Institute of Food, Fisheries and Aquaculture Research (NOFIMA), 9019 Tromsø, Norway
[5]Fundación Canaria Instituto de Investigación Sanitaria de Canarias (FIISC), 35012 Las Palmas de Gran Canaria, Spain
[6]Hospital de Tortosa Verge de la Cinta, 43500 Tortosa, Spain
[7]Departament Medicina i Cirurgia, Universitat Rovira i Virgili, 43003 Tarragona, Spain
[8]Departament Ciències Mèdiques Bàsiques, Universitat Rovira i Virgili, 43003 Tarragona, Spain

Corresponding author: Daniel Ulises Campos-Delgado (ducd@fciencias.uaslp.mx)

This work was supported in part by the Ministerio de Universidades with a Maria Zambrano Fellowship under Grant ING-ARQ/6431200-(SI-1821); in part by Spanish Government and European Union (FEDER funds) through the projects TALENT-HExPERIA (HypErsPEctRal Imaging for Artificial intelligence applications) under Grant PID2020-116417 RB-C42, and OASIS (Open AI-Driven stack para plataformas HPEC mejoradas en sistemas integrados) under Grant PID2023-148285OB-C43; and in part by CONAHCYT by a Doctoral Fellowship under Grant 865747.

**ABSTRACT** The spectral unmixing paradigm is an important analysis tool for hyperspectral (HS) images which allows one to decompose the 2D spatial information from the basic spectral signatures or end-members. In this work, we introduce a semi-supervised perspective for spectral unmixing, where some end-members are known a priori, while the rest are estimated from the HS image. The proposal is relevant in unmixing scenarios where there is only available partial information of end-members, or when the known end-members are not fully representative of the scene. Our formulation simultaneously addresses linear and multilinear mixing models in a unified fashion. The proposed algorithms are referred as ESSEAE (Extended Semi-Supervised End-members and Abundance Extraction) for the linear model, and NESSEAE (Non-linear Extended Semi-Supervised End-members and Abundance Extraction) for the multilinear one. The estimation process is presented as a weighted optimal approximation problem with regularization terms for abundances, end-members and sparse noise components, which is solved by a cyclic coordinate descent optimization (CCDO) scheme. In this work, we derive closed-solutions at each step of the CCDO scheme, and just for the multilinear model, the end-members estimation involves a gradient descent scheme with optimal linear search. We validate first our contributions with synthetic HS images that include Gaussian and sparse noise components to evaluate their robustness, and compare them with supervised and unsupervised perspectives. In addition, we validated the linear scheme with a breast histological sample, and the multilinear approach with the Urban dataset. The use of two datasets from different fields guarantees the generalizability of the proposed formulation. In general, our semi-supervised spectral unmixing schemes provide accurate and robust results with a fast computational time, and as expected, present an overall performance in between the supervised and unsupervised approaches. All scripts for the proposed algorithms are freely available in https://github.com/Nicothe4th/ESSEAE-NESSEAE.

The associate editor coordinating the review of this manuscript and approving it for publication was Kumaradevan Punithakumar.

**INDEX TERMS** Hyperspectral imaging, linear unmixing, nonlinear unmixing, semi-supervised approach, optimization.

## I. INTRODUCTION

### A. MOTIVATION

Hyperspectral (HS) imaging (HSI) is a modality that has revolutionized remote sensing, materials science, medicine, precision agriculture, and surveillance, among other disciplines [1], [2]. In HSI, from a given scene in a 2D spatial domain, the optical spectral properties (reflectance or transmittance) of each spatial point are acquired over hundreds of wavelength channels [3]. In this way, by analyzing the optical reflection or transmission properties of the scene, the materials or basic compounds can be isolated, and their spatial contributions quantified. An important analysis tool for HS images is the spectral unmixing paradigm, which allows to identify the spectral signatures of the basic components or materials in the scene (end-members) and quantify their contributions (abundances) at each spatial point or pixel of the digital image [4].

The relation between end-members and their abundances is provided by a mixing model. In the literature, the most common approach is a linear mixing model (LMM), where at each spatial point, the measured reflectance, absorbance or transmittance is assumed as a linear combination of the end-members, where the abundances scale the contribution of each end-member [5]. On the other hand, there are also nonlinear mixing models (NMM) [6], [7], as the generalized bilinear [8], post-nonlinear and multilinear [9], [10] models. In this sense, the multilinear mixing model (MMM) has the advantage of just relying on single parameter per spatial point or pixel to quantify multiple scattering effects [10]. This simplicity makes MMM more practical compared to other NMM, which typically require more complex formulations and multiple parameters to model interactions. Another recent trend in unmixing methodologies is deep learning [11], where convolutional neural networks and auto-encoders have been extensively studied, and recently physics-based and data-driven approaches have also been proposed [12]. Nonetheless, in this contribution, we will focus on unmixing methods based on mathematical models since they provide an appropriate framework for our technical derivations.

### B. SPECTRAL UNMIXING

Spectral unmixing algorithms could be classified with respect to the amount of previous knowledge we had about the end-members [13], as shown in Fig. 1. In a supervised approach, all possible materials and their spectral signatures are known in advance. So, the complete set of end-members is assumed to be fixed in the HS image, and just the abundance maps are estimated by the unmixing algorithm. In this scenario, a library of end-members is usually considered, so a sparse condition is adopted during the abundances estimation. Other more challenging approach is an unsupervised perspective, where the end-members and their abundances are jointly estimated from a HS image [4]. Finally, if there is partial knowledge of the end-members in the scene, so just some components or materials and their spectral signatures are known in advance, but some others have to be identified from the image data, then a semi-supervised approach (SSA) is pursued [14].

Another approach, called also semi-supervised unmixing, involves using a large library of potential end-members [15]. This library is then refined by selecting only the end-members that best explain the observed data. Finally, the fractional contributions of these selected end-members are estimated.

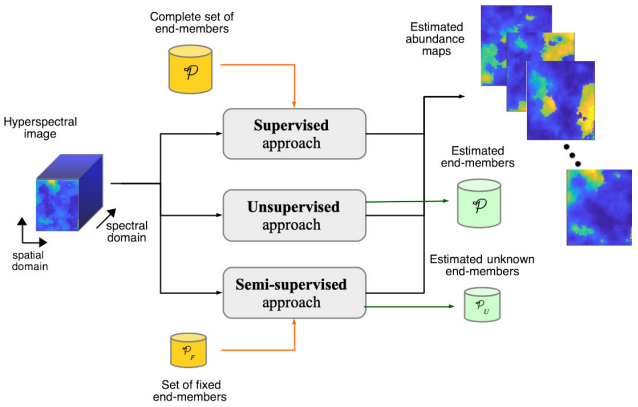


**FIGURE 1.** Schematic of the diverse perspectives of spectral unmixing: (i) Supervised, (ii) unsupervised or unsupervised, and (iii) semi-supervised.

With respect to the literature in spectral unmixing approaches, either supervised or unsupervised methodologies have been proposed in state-of-the-art [3], [5], [6]. For a supervised perspective and a LMM, methodologies that consider optimal norm approximations, different noise sources in the HS image, and promote sparseness in the estimated abundances or spatial coherence, have been recently studied: (i) unmixing that considers Gaussian and sparse noise components with joint sparsity of the abundance maps [16], (ii) low-rank and sparse estimations of the abundances with also Gaussian and sparse noise terms [17], (iii) coarse and high resolution approximations with sparse regression for the abundances by alternating direction method of multipliers [18], and (iv) robust unmixing with three types of noise components (Gaussian, sparse and strip) based on constrained convex optimization [19].

Now, with an unsupervised approach and a LMM, the most common approach is based on non-negative matrix factorization (NNMF) at its variations [20]. The following methods have been introduced for unsupervised linear unmixing: (i) NNMF with a minimum volume condition on the estimated end-members [21], (ii) extended unsupervised end-members and abundance extraction (EBEAE)

by constrained quadratic optimization and alternated least squares [22], (iii) graph-based framework with an alternating direction method of multipliers by applying Merriman-Bence-Osher scheme [23], and (iv) sparsity-enhanced convolutional decomposition to address simultaneously spatial-spectral information [24].

For a LMM, a Bayesian framework was suggested for spectral unmixing by a selection of end-members inside a library in [15], where this scheme is denoted as semi-supervised. In this context, recent contributions are described next: (i) mutual coherence reduction method for dictionary pruning of end-members [25], (ii) spectral and spatial priors by matrix factorization [26], and (iii) non-convex optimization by modifying the LMM [27].

Meanwhile, the literature in spectral unmixing with a MMM is not as extensive as with a linear model. Hence, with a supervised approach and a MMM, the work in [10] proposed the unmixing by using an optimal approximation problem with the Euclidean norm. Meanwhile, unsupervised unmixing with a MMM was studied recently looking to consider different noise sources and spatial coherence by the following frameworks: (i) unsupervised approach based on constrained quadratic optimization [28], (ii) graph-regularized optimization to provide spatial coherence in the abundance maps [29], (iii) robust unmixing approach by including the $l2,1$ norm in the error fidelity and sparseness of the abundances [30], and (iv) a nonlinear extension of EBEAE (NEBEAE) by considering a cyclic coordinate descent optimization (CCDO) scheme and constrained quadratic optimization [31].

### C. CONTRIBUTION

By considering linear and nonlinear spectral unmixing, in our review of the state-of-the-art, we have not identified schemes that address SSA (i.e. some end-members are known & fixed initially, and some unknown are estimated during unmixing) although the research problem can have many potential applications. One possible aplication is in a scene where some materials and their spectral signatures are present and known before hand, but some other components have not been identified. Another possible application is to distinguish spectral variability in a HS image, where, in addition to a fixed library of known end-members, extra ones could be estimated from the dataset. In fact, the only reference close to SSA focused on a LMM in [14], where the synthesis scheme is formulated by an optimal approximation problem and block cyclic descent algorithm. In [14], there are no explicit constraints in the end members and their abundances, and during the optimization process, penalty functions are added to enforce the normalization conditions.

In this context, we introduce our technical contribution, which is based on a SSA to address LMM and MMM in a unified fashion. Moreover, in our SSA paradigm, we take into account Gaussian and sparse noise terms to derive robust spectral unmixing schemes that take into account the induced distortion by instrumentation and environmental effects [32]. Our mathematical formulations depart from our early work in EBEAE [22] and NEBEAE [31], where now some end-members are previously known, and the proposed algorithms are referred to as: (a) ESSEAE, and (b) NESSEAE. Our proposals of spectral unmixing are approached as weighted optimal approximation problems with regularization terms for abundances, end-members and sparse noise components, where the Euclidean and $L_1$ norm are used in these terms. To derive our solutions, we rely in the CCDO scheme to iteratively optimize one variable while the rest are kept fixed. In this framework, for ESSEAE, all the resulting optimization problems have closed-solutions, but for NESSEAE, the end-members estimation uses a gradient descent update with optimal linear search. In our validation process, we use synthetic HS images emulating the absorption properties of biological tissue under Gaussian and sparse noise components by comparing supervised, unsupervised and our SSA schemes. Finally, we also considered validations with real-world HS images of a breast histological sample, and Urban dataset.

The rest of the paper is organized as follows. First, the mathematical notation is introduced, which will be used during the derivations of the unified spectral unmixing schemes based on a SSA. Next, in Section II, the problem of semi-supervised spectral unmixing is formulated for LMM and MMM, where the solutions for ESSEAE and NESSEAE optimization problems for abundances, sparse noise matrix, end-members, and nonlinear interaction levels are formally derived. At the end of Section II, implementation guidelines are introduced for the proposed algorithms. Section III introduces the validation methodology that considers performance metrics, and synthetic and real-world HS datasets. The results for the synthetic and real-world datasets and their discussion are introduced in Section IV. Finally, in Section IV, the conclusions are presented, as well as, some limitations and future research lines.

### D. NOTATION

The notation used in this work is described in the following. Scalars, vectors and matrices are denoted by italic, boldface lower-case, and boldface upper-case letters, respectively. A $L$-dimensional vector with unitary entries and the corresponding identity matrix are defined as $\mathbf{1}_L$, and $\mathbf{I}_L$, respectively. For a vector $\mathbf{x}$, its transpose is represented by $\mathbf{x}^\top$, its $l$-th component by $(\mathbf{x})_l$, its Euclidean norm by $\|\mathbf{x}\| = \sqrt{\sum_l (\mathbf{x})_l^2}$, the $L_1$ norm by $\|\mathbf{x}\|_1 = \sum_l |\mathbf{x}_l|$, and $|\mathbf{x}|$ represents a new vector obtained by applying the absolute value per component. For two vectors $\mathbf{x}$ and $\mathbf{y}$, $\mathbf{x} \odot \mathbf{y}$ defines the Hadamard product. For a matrix $\mathbf{X}$, $\|\mathbf{X}\|_F = \sqrt{\text{Tr}(\mathbf{X}\mathbf{X}^\top)}$ denotes its Frobenius norm, where $\text{Tr}(\cdot)$ expresses the trace operation; and $\text{rank}(\mathbf{X})$ the maximum number of linearly independent columns in $\mathbf{X}$. A diagonal matrix with elements in $\mathbf{x}$ is defined as $\text{diag}(\mathbf{x})$, and for a symmetric matrix $\mathbf{X}$, $\lambda_{min}(\mathbf{X})$ represents its minimum eigenvalue. For a set $\mathcal{X}$, $\text{card}(\mathcal{X})$ denotes its cardinality.

## II. SEMI-SUPERVISED SPECTRAL UNMIXING

### A. PROBLEM FORMULATION

A HS image $\mathbf{H} \in \mathbb{R}^{L\times X\times Y}$ is studied, where $L$ is the number of spectral channels and $X \times Y$ denotes the spatial dimensions. Thus, $K = X \cdot Y$ refers to the total number of spatial points or pixels in the image. In our methodology, the columns in $\mathbf{H}$ are concatenated to obtain a 2D matrix $\mathbf{Z} = [\mathbf{z}_1 \ \cdots \ \mathbf{z}_K] \in \mathbb{R}^{L\times K}$, which are denoted as $\mathbf{z}_k \in \mathbb{R}^L$ where $k \in \mathcal{K} = \{1, \ldots, K\}$. Hence, in our framework, we do not exploit the spatial correlations in the image. The spectral response per channel and spatial point is assumed a non-negative number, so $\mathbf{z}_k \geq 0 \ \forall k \in \mathcal{K}$ (i.e. the inequality is interpreted component-wise). Without loss of generality, all the measurements $\mathcal{Z} = \{\mathbf{z}_1, \ldots, \mathbf{z}_K\}$ are scaled to sum-to-one:

$$\mathbf{y}_k \triangleq \frac{1}{\mathbf{1}_L^\top \mathbf{z}_k}\mathbf{z}_k \quad \forall k \in \mathcal{K}, \tag{1}$$

so the set of scaled measurements is denoted as $\mathcal{Y} = \{\mathbf{y}_1, \ldots, \mathbf{y}_K\}$. In the following derivations, we will address in a unified fashion the corresponding representations for LMM and MMM based on our previous contributions [22], [31]. We will define the following sets $\Omega_P$ and $\Omega_A$ related to the spectral responses and spatial contributions, respectively:

$$\Omega_P = \{\mathbf{p} \in \mathbb{R}^L \ : \ \mathbf{p} \geq 0 \quad \& \quad \mathbf{1}_L^\top \mathbf{p} = 1\}, \tag{2}$$

$$\Omega_A = \{\boldsymbol{\alpha} \in \mathbb{R}^N \ : \ \boldsymbol{\alpha} \geq 0 \quad \& \quad \mathbf{1}_N^\top \boldsymbol{\alpha} = 1\}. \tag{3}$$

In general, a LMM of $N$-th order relates a set of end-members $\mathcal{P} = \{\mathbf{p}_1, \ldots, \mathbf{p}_N\}$ ($\mathbf{p}_n \in \Omega_P \ \forall n \in \mathcal{N} = \{1, \ldots, N\}$), which are common to the whole image $\mathbf{H}$ and characterize the spectral responses of the basic components, to their spatial contributions or abundances $\mathcal{A} = \{\boldsymbol{\alpha}_1, \ldots, \boldsymbol{\alpha}_K\}$ ($\boldsymbol{\alpha}_k \in \Omega_A \ \forall k \in \mathcal{K}$). In addition, for a MMM, the model takes into account a set of non-linear interaction levels $\mathcal{D} = \{d_1, \ldots, d_K\}$ ($d_k \in (-\infty, 1] \ \forall k \in \mathcal{K}$), which are related to multiple scattering effects [10]. In this way, the $k$-th scaled measurement is represented as:

$$\mathbf{y}_k = \begin{cases} \mathbf{P}\boldsymbol{\alpha}_k + \mathbf{n}_k + \mathbf{v}_k, & \text{(LMM)} \\ (1-d_k)(\mathbf{P}\boldsymbol{\alpha}_k) + d_k\,(\mathbf{P}\boldsymbol{\alpha}_k) \odot \mathbf{z}_k & \\ \quad +\mathbf{n}_k + \mathbf{v}_k. & \text{(MMM)} \end{cases} \tag{4}$$

where $\mathbf{P} = [\mathbf{p}_1 \ \cdots \ \mathbf{p}_N] \in \mathbb{R}^{L\times N}$ is the matrix of end-members, with $\mathbf{p}_n \in \mathcal{P}$ as the $n$-th end-member $\forall n \in \mathcal{N}$, vector $\boldsymbol{\alpha}_k \in \mathcal{A}$ contains the abundances at the $k$-th measurement, $\mathbf{n}_k \in \mathbb{R}^L$ denotes a sparse noise vector, and $\mathbf{v}_k \in \mathbb{R}^L$ is white noise. The elements in $\mathbf{v}_k$ are assumed zero-mean and i.i.d. with a Gaussian distribution ($\mathbf{1}_L^\top \mathbf{v}_k \approx 0$). The set $\mathcal{P}$ is linearly independent, i.e. rank($\mathbf{P}$) $= N$. Now, since all end-members belong to $\Omega_P$ and as a consequence $\mathbf{P}^\top \mathbf{1}_L = \mathbf{1}_N$, the normalization condition on the scaled measurements $\mathcal{Y}$ imposes the following constraint for the abundances and sparse noise terms:

$$\mathbf{1}_L^\top \mathbf{y}_k = \boldsymbol{\delta}_k^\top \boldsymbol{\alpha}_k + \mathbf{1}_L^\top \mathbf{n}_k = 1.0 \quad \forall k \in \mathcal{K}, \tag{5}$$

where $\boldsymbol{\delta}_k \in \mathbb{R}^N$ is adjusted according to the mixing model:

$$\boldsymbol{\delta}_k = \begin{cases} \mathbf{1}_N, & \text{(LMM)} \\ (1-d_k)\mathbf{1}_N + d_k \mathbf{P}^\top \mathbf{z}_k. & \text{(MMM)} \end{cases} \tag{6}$$

In this contribution, and in contrast to previous approaches from the literature, we follow a SSP with respect to a prior knowledge of end-members, so it is assumed that a subset $\mathcal{P}_F \subset \mathcal{P}$ is known or fixed during the estimation process, where card($\mathcal{P}_F$) $= F < N$. The rest of end-members $U = N - F$ are estimated during the unmixing scheme. So the end-members matrix $\mathbf{P}$ is divide into a fixed part $\mathbf{P}_F \in \mathbb{R}^{L\times F}$ and unknown one $\mathbf{P}_U \in \mathbb{R}^{L\times U}$, where without a loss of generality, the $F$ first columns are assigned to the fixed elements, and the last $U$ to the unknown:

$$\mathbf{P} = \left[\underbrace{\mathbf{p}_1 \ldots \mathbf{p}_F}_{\mathbf{P}_F} \underbrace{\mathbf{p}_{F+1} \ldots \mathbf{p}_{F+U}}_{\mathbf{P}_U}\right] = [\mathbf{P}_F \ \mathbf{P}_U], \tag{7}$$

i.e. $\mathcal{P}_F = \{\mathbf{p}_1, \ldots, \mathbf{p}_F\}$, and $N$ = rank ($\mathbf{P}_F$) + rank ($\mathbf{P}_U$). As the end-members matrix $\mathbf{P}$, for the $k$-th spatial location, the abundances vector is organized in the same fashion, i.e. the first $F$ components $\boldsymbol{\alpha}_{F,k} \in \mathbb{R}^F$ are associated to the fixed end-members, and the last $U$ abundances $\boldsymbol{\alpha}_{U,k} \in \mathbb{R}^U$ to the unknown ones:

$$\boldsymbol{\alpha}_k = \left[\underbrace{\alpha_{1,k} \ldots \alpha_{F,k}}_{\boldsymbol{\alpha}_{F,k}} \underbrace{\alpha_{F+1,k} \ldots \alpha_{F+U,k}}_{\boldsymbol{\alpha}_{U,k}}\right]^\top = \begin{bmatrix}\boldsymbol{\alpha}_{F,k} \\ \boldsymbol{\alpha}_{U,k}\end{bmatrix}. \tag{8}$$

By considering this SSP approach, a new representation of the $k$-th scaled measurement is given by

$$\mathbf{y}_k = \begin{cases} \mathbf{P}_F\boldsymbol{\alpha}_{F,k} + \mathbf{P}_U\boldsymbol{\alpha}_{U,k} + \mathbf{n}_k + \mathbf{v}_k, & \text{(LMM)} \\ (1-d_k)(\mathbf{P}_F\boldsymbol{\alpha}_{F,k}) + (1-d_k)(\mathbf{P}_U\boldsymbol{\alpha}_{U,k}) & \\ \quad +d_k\left(\mathbf{P}_F\boldsymbol{\alpha}_{F,k}\right) \odot \mathbf{z}_k & \\ \quad +d_k\left(\mathbf{P}_U\boldsymbol{\alpha}_{U,k}\right) \odot \mathbf{z}_k + \mathbf{n}_k + \mathbf{v}_k. & \text{(MMM)} \end{cases} \tag{9}$$

Under this mathematical framework and departing from [22] and [31], we introduce two synthesis problems for LMM and MMM scenarios: (a) ESSEAE and (b) NESSEAE. For both optimization problems, the cost function is introduced in a unified fashion with four components: (i) Error fidelity term, (ii) abundances entropy, (iii) sparse noise regularization, and (iv) end-members similarity term [22], [31]:

$$\begin{aligned} \min \quad & \underbrace{\frac{1}{2K}\text{RET}}_{(i)} \underbrace{-\frac{\mu}{2K}\sum_{k\in\mathcal{K}}\|\boldsymbol{\alpha}_k\|^2}_{(ii)} + \underbrace{\frac{\lambda}{K}\sum_{k\in\mathcal{K}}\|\mathbf{n}_k\|_1}_{(iii)} \\ & \underbrace{+\frac{\rho}{2\vartheta}\left(\sum_{f=1}^{F}\sum_{u=F+1}^{F+U}\|\mathbf{p}_f-\mathbf{p}_u\|^2+\sum_{u=F+1}^{F+U-1}\sum_{j=n+1}^{F+U}\|\mathbf{p}_u-\mathbf{p}_j\|^2\right)}_{(iv)}, \end{aligned} \tag{10}$$

where based on the mixing model, the fidelity error can take two possible outcomes:

$$\text{RET} = \begin{cases} \displaystyle\sum_{k\in\mathcal{K}} \frac{\|\mathbf{y}_k - \mathbf{P}\boldsymbol{\alpha}_k - \mathbf{n}_k\|^2}{\|\mathbf{y}_k\|^2}, & \text{(LMM)} \\ \displaystyle\sum_{k\in\mathcal{K}} \frac{\|\mathbf{y}_k - (1-d_k)\mathbf{P}\boldsymbol{\alpha}_k - d_k\,(\mathbf{P}\boldsymbol{\alpha}_k)\odot\mathbf{z}_k - \mathbf{n}_k\|^2}{\|\mathbf{y}_k\|^2}, & \text{(MMM)} \end{cases} \tag{11}$$

and

$$\vartheta = \begin{cases} (N-1)+\cdots+1 & N\geq 3, \\ 1 & N=2, \end{cases} \tag{12}$$

such that $\boldsymbol{\alpha}_k \geq 0\ \forall k$ and (5) are satisfied, and $\mathbf{p}_{F+u} \in \Omega_P$ $\forall u \in \mathcal{U} = \{1,\ldots,U\}$ is also fulfilled. With respect to the similarity term among end-members in (iv), this formulation is different to [22] and [31], since the end-members in $\mathcal{P}_F$ are known already, so they are not estimated by ESSEAE or NESSEAE. In this way, the distance terms that involve elements inside $\mathcal{P}_F$ are discarded. For ESSEAE, the variables in (10) are $\mathbf{P}_U$, $\{\boldsymbol{\alpha}_k\}$ and $\{\mathbf{n}_k\}$, and for NESSEAE additionally includes $\{d_k\}$. Now, a CCDO method solves (10) iteratively by optimizing one type of variable at a time while keeping the others fixed. Except for the step for the updatable end-members estimation, the end-members matrix $\mathbf{P}$ is always considered as a whole (fixed and updatable components) during the mathematical formulations. The solutions for each individual optimization problem are described below.

### B. ABUNDANCES ESTIMATION

In the cost function in (10), no spatial relation is considered among the abundances. As a result, the abundances at each spatial location or pixel can be solved independently. Hence, the corresponding cost function for the abundance vector at $k$-th spatial $\boldsymbol{\alpha}_k$ is expressed as:

$$\min_{\boldsymbol{\alpha}_k\geq 0,\ \boldsymbol{\delta}_k^\top\boldsymbol{\alpha}_k = 1-\mathbf{1}_L^\top\mathbf{n}_k} \frac{1}{2}\frac{\|\mathbf{s}_k - \boldsymbol{\Lambda}_k\boldsymbol{\alpha}_k\|^2}{\|\mathbf{y}_k\|^2} - \frac{\mu}{2}\|\boldsymbol{\alpha}_k\|^2 \quad \forall k\in\mathcal{K}, \tag{13}$$

where $\mathbf{s}_k = \mathbf{y}_k - \mathbf{n}_k$ refers to the measurement without the sparse noise component, and

$$\boldsymbol{\Lambda}_k \triangleq \begin{cases} \mathbf{P}, & \text{(LMM)} \\ \mathbf{P}\odot\left[(1-d_k)\mathbf{1}_{L\times N} + d_k\mathbf{z}_k^\top\mathbf{1}_N\right]. & \text{(MMM)} \end{cases} \tag{14}$$

Following the procedure in [22], the hyper-parameter $\mu$ in (13) is redefined to have a weight specific for the $k$-th spatial location as

$$\mu = \bar{\mu}\cdot\frac{\lambda_{min}(\boldsymbol{\Lambda}_k^\top\boldsymbol{\Lambda}_k)}{\|\mathbf{y}_k\|^2}, \tag{15}$$

where $\bar{\mu}\in[0,1)$ is the new normalized hyper-parameter. The solution to the constrained quadratic optimization in (13) is given by:

$$\boldsymbol{\alpha}_k = \boldsymbol{\Theta}_k\cdot\left(\boldsymbol{\Lambda}_k^\top\mathbf{s}_k - \frac{\mathbf{s}_k^\top\boldsymbol{\Lambda}_k\boldsymbol{\Theta}_k\boldsymbol{\delta}_k - \left[1-\mathbf{1}_L^\top\mathbf{n}_k\right]}{\boldsymbol{\delta}_k^\top\boldsymbol{\Theta}_k\boldsymbol{\delta}_k}\mathbf{1}_N\right), \tag{16}$$

where $\boldsymbol{\Theta}_k \triangleq \left(\boldsymbol{\Lambda}_k^\top\boldsymbol{\Lambda}_k - \bar{\mu}\lambda_{min}(\boldsymbol{\Lambda}_k^\top\boldsymbol{\Lambda}_k)\mathbf{I}_N\right)^{-1} \in \mathbb{R}^{N\times N}$.

### C. SPARSE NOISE ESTIMATION

From (10), for the $k$-th measurement, the sparse noise term $\mathbf{n}_k$ is estimated by the following problem:

$$\min_{\mathbf{n}_k\geq 0}\ \|\mathbf{n}_k\|_1 + \frac{1}{2\lambda}\frac{\|\mathbf{n}_k - \mathbf{e}_k\|^2}{\|\mathbf{y}_k\|^2} \quad \forall k\in\mathcal{K}, \tag{17}$$

where the $k$-th error $\mathbf{e}_k$ not related to the mixing model is given by:

$$\mathbf{e}_k = \begin{cases} \mathbf{y}_k - \mathbf{P}\boldsymbol{\alpha}_k, & \text{(LMM)} \\ \mathbf{y}_k - (1-d_k)\mathbf{P}\boldsymbol{\alpha}_k - d_k(\mathbf{P}\boldsymbol{\alpha}_k)\odot\mathbf{z}_k. & \text{(MMM)} \end{cases} \tag{18}$$

Now, the optimization in (17) involves a $L_1$-regularized problem. Therefore, a solution is reached by a shrinkage operation [33]:

$$\mathbf{n}_k = \text{sign}(\mathbf{e}_k)\odot\max\left\{0,\ |\mathbf{e}_k| - \lambda\|\mathbf{y}_k\|^2\right\}, \tag{19}$$

where sign$(\cdot)$ and max$(\cdot)$ are applied component-wise. In (19), there is no coupling among all spatial points, so a parallel computation could be followed to speed up the estimation process:

$$\mathbf{N} = \text{sign}(\mathbf{E})\odot\max\left(\mathbf{0},\ |\mathbf{E}| - \lambda\mathbf{Y}_e\right), \tag{20}$$

where $\mathbf{N} = [\mathbf{n}_1\ \cdots\ \mathbf{n}_K]\in\mathbb{R}^{L\times K}$ is the sparse noise matrix, $\mathbf{E} = [\mathbf{e}_1\ \cdots\ \mathbf{e}_K]\in\mathbb{R}^{L\times K}$ the estimation error matrix, and $\mathbf{Y}_e = \left[\|\mathbf{y}_1\|^2\cdot\mathbf{1}_L\ \cdots\ \|\mathbf{y}_K\|^2\cdot\mathbf{1}_L\right]\in\mathbb{R}^{L\times K}$.

### D. END-MEMBERS ESTIMATION

The cost-function in (10) is re-written in a matrix notation with respect to the updatable end-members variable $\mathbf{P}_U$, and the fixed ones $\mathbf{P}_F$:

$$\min_{\mathbf{P}_U}\frac{1}{2K}\text{RET} + \frac{\rho}{2\vartheta}\left\{\text{Tr}\left(\mathbf{P}_U\boldsymbol{\Theta}_1\mathbf{P}_F^\top\right) + \text{Tr}\left(\mathbf{P}_U\boldsymbol{\Theta}_2\mathbf{P}_U^\top\right)\right\}, \tag{21}$$

such that $\mathbf{P}_U \geq 0$ and $\mathbf{P}_U^\top\mathbf{1}_L = \mathbf{1}_U$, i.e. each column in $\mathbf{P}_U$ belongs to $\Omega_P$, where the following matrices $\boldsymbol{\Theta}_1$ and $\boldsymbol{\Theta}_2$ are defined as:

$$\boldsymbol{\Theta}_1 = -2\left(\mathbf{1}_U\mathbf{1}_F^\top\right)\in\mathbb{R}^{U\times F}, \tag{22}$$

$$\boldsymbol{\Theta}_2 = N\mathbf{I}_U - \mathbf{1}_U\mathbf{1}_U^\top\in\mathbb{R}^{U\times U}, \tag{23}$$

where it is observed that $\boldsymbol{\Theta}_2$ is a symmetric matrix. In the Appendix, we provide a detailed derivation for the end-members similarity term in (10), and the corresponding optimization scheme in (21).

### 1) LINEAR MIXING MODEL

For the LMM, the constrained optimization problem with respect to $\mathbf{P}_U$ is quadratic and admits a closed-solution, so we can define in matrix notation the fidelity error related to the fixed end-members and sparse noise term $\mathbf{X} \in \mathbb{R}^{L\times K}$ as:

$$\mathbf{X} = \mathbf{Y} - \mathbf{P}_F\mathbf{A}_F - \mathbf{N}, \tag{24}$$

and adding a Lagrange operator $\boldsymbol{\chi} \in \mathbb{R}^U$ to include the sum-to-one restriction, the minimization problem in (21) is formulated as:

$$\min_{\mathbf{P}_U} \mathrm{J}_{LMM} \tag{25}$$

$$\begin{aligned}\mathrm{J}_{LMM} \triangleq\ & \frac{1}{2}\mathrm{Tr}\left\{(\mathbf{X}-\mathbf{P}_U\mathbf{A}_U)\mathbf{W}(\mathbf{X}-\mathbf{P}_U\mathbf{A}_U)^\top\right\} \\ & + \frac{\rho}{2\vartheta}\left\{\mathrm{Tr}\left(\mathbf{P}_U\boldsymbol{\Theta}_1\mathbf{P}_F^\top\right) + \mathrm{Tr}\left(\mathbf{P}_U\boldsymbol{\Theta}_2\mathbf{P}_U^\top\right)\right\} \\ & + \boldsymbol{\chi}^\top\left(\mathbf{P}_U^\top\mathbf{1}_L - \mathbf{1}_U\right),\end{aligned} \tag{26}$$

where

$$\mathbf{A}_F = [\boldsymbol{\alpha}_{F,1}\ \cdots\ \boldsymbol{\alpha}_{F,K}] \in \mathbb{R}^{F\times K}, \tag{27}$$

$$\mathbf{A}_U = [\boldsymbol{\alpha}_{U,1}\ \cdots\ \boldsymbol{\alpha}_{U,K}] \in \mathbb{R}^{U\times K}, \tag{28}$$

$$\mathbf{W} = \frac{1}{K}\mathrm{diag}\left([1/\|\mathbf{y}_1\|^2\ \cdots\ 1/\|\mathbf{y}_K\|^2]\right) \in \mathbb{R}^{K\times K}, \tag{29}$$

denote the abundance matrices of the fixed and unknown end-members, respectively, and a weight matrix for the fidelity error. The solution of (25) is given by solving the stationary conditions for the partial differential equations:

$$\begin{aligned}\frac{\partial \mathrm{J}_{LMM}}{\partial \mathbf{P}_U} =\ & -\mathbf{X}\mathbf{W}\mathbf{A}_U^\top + \mathbf{P}_U\mathbf{A}_U\mathbf{W}\mathbf{A}_U^\top + \frac{\rho}{2\vartheta}\mathbf{P}_F\boldsymbol{\Theta}_1^\top \\ & + \frac{\rho}{\vartheta}\mathbf{P}_U\boldsymbol{\Theta}_2^\top + \mathbf{1}_L\boldsymbol{\chi}^\top = 0,\end{aligned} \tag{30}$$

$$\frac{\partial \mathrm{J}}{\partial \boldsymbol{\chi}} = \mathbf{P}_U^\top\mathbf{1}_L - \mathbf{1}_U = 0. \tag{31}$$

By solving for $\mathbf{P}_U$ in (30), we obtain:

$$\mathbf{P}_U = \left[\mathbf{X}\mathbf{W}\mathbf{A}_U^\top - \frac{\rho}{2\vartheta}\mathbf{P}_F\boldsymbol{\Theta}_1^\top - \mathbf{1}_L\boldsymbol{\chi}^\top\right]\boldsymbol{\Phi}^{-1}, \tag{32}$$

where $\boldsymbol{\Phi} \triangleq \left[\mathbf{A}_U\mathbf{W}\mathbf{A}_U^\top + \frac{\rho}{\vartheta}\boldsymbol{\Theta}_2^\top\right] \in \mathbb{R}^{U\times U}$. Now with a direct substitution of (32) in (31), $\boldsymbol{\chi}$ is obtained as:

$$\boldsymbol{\chi} = \frac{1}{L}\left(\mathbf{A}_U\mathbf{W}\mathbf{X}^\top - \frac{\rho}{2\vartheta}\boldsymbol{\Theta}_1\mathbf{P}_F^\top\right)\mathbf{1}_L - \frac{1}{L}\boldsymbol{\Phi}^\top\mathbf{1}_U. \tag{33}$$

Finally, using (33) to solve (30) for $\mathbf{P}_U$, it is deduced the optimal solution:

$$\begin{aligned}\mathbf{P}_U =\ & \left(\mathbf{I}_L - \frac{\mathbf{1}_L\mathbf{1}_L^\top}{L}\right)\left(\mathbf{X}\mathbf{W}\mathbf{A}_U^\top - \frac{\rho}{2\vartheta}\mathbf{P}_F\boldsymbol{\Theta}_1^\top\right)\boldsymbol{\Phi}^{-1} \\ & + \frac{\mathbf{1}_L\mathbf{1}_U^\top}{L}.\end{aligned} \tag{34}$$

### 2) MULTILINEAR MIXING MODEL

Meanwhile, for the MMM perspective, a closed-solution is not viable, so a gradient descent approach with an optimized linear search is considered, as in [31]. To derive this scheme, the optimization process in (21) is rewritten in terms of the unknown and fixed variables:

$$\min_{\mathbf{P}_U} \mathrm{J}_{MMM} \tag{35}$$

such that

$$\begin{aligned}\mathrm{J}_{MMM} \triangleq\ & \sum_{k\in\mathcal{K}} \frac{\|\mathbf{v}_k - (1-d_k)\mathbf{P}_U\boldsymbol{\alpha}_{U,k} - d_k\left(\mathbf{P}_U\boldsymbol{\alpha}_{U,k}\right)\odot\mathbf{z}_k\|^2}{2K\|\mathbf{y}_k\|^2}, \\ & + \frac{\rho}{2\vartheta}\left\{\mathrm{Tr}\left(\mathbf{P}_U\boldsymbol{\Theta}_1\mathbf{P}_F^\top\right) + \mathrm{Tr}\left(\mathbf{P}_U\boldsymbol{\Theta}_2\mathbf{P}_U^\top\right)\right\},\end{aligned} \tag{36}$$

$$\begin{aligned}=\ & \sum_{k\in\mathcal{K}} \frac{\|\mathbf{v}_k\|^2 - 2\mathbf{v}_k^\top\mathbf{M}_k\mathbf{P}_U\boldsymbol{\alpha}_{U,k} + \boldsymbol{\alpha}_{U,k}^\top\mathbf{P}_U^\top\mathbf{M}_k^\top\mathbf{M}_k\mathbf{P}_U\boldsymbol{\alpha}_{U,k}}{2K\|\mathbf{y}_k\|^2} \\ & + \frac{\rho}{2\vartheta}\left\{\mathrm{Tr}\left(\mathbf{P}_U\boldsymbol{\Theta}_1\mathbf{P}_F^\top\right) + \mathrm{Tr}\left(\mathbf{P}_U\boldsymbol{\Theta}_2\mathbf{P}_U^\top\right)\right\},\end{aligned} \tag{37}$$

where

$$\mathbf{v}_k \triangleq \mathbf{y}_k - (1-d_k)\mathbf{P}_F\boldsymbol{\alpha}_{F,k} - d_k\left(\mathbf{P}_F\boldsymbol{\alpha}_{F,k}\right)\odot\mathbf{z}_k - \mathbf{n}_k, \tag{38}$$

$$\mathbf{M}_k \triangleq (1-d_k)\mathbf{I}_L - d_k\mathrm{diag}(\mathbf{z}_k) \in \mathbb{R}^{L\times L}. \tag{39}$$

So, by taking the partial derivative of $\mathrm{J}_{MMM}$ with respect to $\mathbf{P}_U$, we obtain the update step

$$\begin{aligned}\frac{\partial \mathrm{J}_{MMM}}{\partial \mathbf{P}_U} =\ & \sum_{k\in\mathcal{K}}\left\{-\frac{\mathbf{M}_k^\top\mathbf{v}_k\boldsymbol{\alpha}_{U,k}^\top}{K\|\mathbf{y}_k\|^2} + \frac{\mathbf{M}_k^\top\mathbf{M}_k\mathbf{P}_U\boldsymbol{\alpha}_{U,k}\boldsymbol{\alpha}_{U,k}^\top}{K\|\mathbf{y}_k\|^2}\right\} \\ & + \frac{\rho}{2\vartheta}\left\{\mathbf{P}_F\boldsymbol{\Theta}_1^\top + 2\mathbf{P}_U\boldsymbol{\Theta}_2\right\} \triangleq \boldsymbol{\Gamma} \in \mathbb{R}^{L\times U}.\end{aligned} \tag{40}$$

As a next step, the optimal step $\gamma^l$ in a linear search is derived at $l$-th iteration of the gradient descent scheme:

$$\mathbf{P}_U^{l+1} = \mathbf{P}_U^l - \gamma^l\boldsymbol{\Gamma}^l \qquad l \geq 0. \tag{41}$$

So, by assuming that $\mathbf{P}_U^l$ and $\boldsymbol{\Gamma}^l$ are known, the following unconstrained optimization process is proposed at $l$-iteration:

$$\min_{\gamma^l} \tilde{\mathrm{J}}_{MMM}, \tag{42}$$

where $\tilde{\mathrm{J}}_{MMM}$ is defined in (43), as shown at the bottom of the next page. A direct substitution shows that the previous optimization problem is quadratic in $\gamma^l$, so the following stationary condition provides the solution:

$$\frac{\partial \tilde{\mathrm{J}}_{MMM}}{\partial \gamma^l} = 0, \tag{44}$$

i.e. $\gamma^l = \max\left(0, \frac{\gamma_{num}^l}{\gamma_{den}^l}\right)$ such that:

$$\gamma_{num}^l = \sum_{k\in\mathcal{K}} \frac{(\boldsymbol{\alpha}_{U,k}^l)^\top(\boldsymbol{\Gamma}^l)^\top(\mathbf{M}_k^l)^\top(\mathbf{M}_k^l)(\mathbf{P}_U^l\boldsymbol{\alpha}_{U,k}^l - \mathbf{v}_k^l)}{K\|\mathbf{y}_k\|^2}$$

$$+\frac{\rho}{\vartheta}\,\mathrm{Tr}\left(\boldsymbol{\Gamma}^l\boldsymbol{\Theta}_2(\mathbf{P}_U^l)^\top\right)+\frac{\rho}{2\vartheta}\,\mathrm{Tr}\left(\boldsymbol{\Gamma}^l\boldsymbol{\Theta}_1(\mathbf{P}_F^l)^\top\right), \tag{45}$$

$$\gamma_{den}^l=\sum_{k\in\mathcal{K}}\frac{(\boldsymbol{\alpha}_{U,k}^l)^\top(\boldsymbol{\Gamma}^l)^\top(\mathbf{M}_k^l)^\top\mathbf{M}_k^l\boldsymbol{\Gamma}^l\boldsymbol{\alpha}_{U,k}^l}{K\|\mathbf{y}_k\|^2}+\frac{\rho}{\vartheta}\mathrm{Tr}\left(\boldsymbol{\Gamma}^l\boldsymbol{\Theta}_2(\boldsymbol{\Gamma}^l)^\top\right), \tag{46}$$

by recalling that $\mathrm{Tr}(\mathbf{V})=\mathrm{Tr}(\mathbf{V}^\top)$, where $\mathbf{V}$ is any square real matrix.

### E. ESTIMATION OF NONLINEAR INTERACTION LEVEL

Finally, just for the MMM perspective, the nonlinear interaction levels $\{d_k\}$ can be solved in a decoupled fashion at each spatial location independently. From (10), the optimization problem for the $k$-th nonlinear interaction level $d_k$ is given by:

$$\min_{d_k\in(-\infty,1]}\frac{1}{2}\|\mathbf{y}_k-(1-d_k)\mathbf{P}\boldsymbol{\alpha}_k-d_k\,(\mathbf{P}\boldsymbol{\alpha}_k)\odot\mathbf{z}_k-\mathbf{n}_k\|^2\quad\forall k\in\mathcal{K}, \tag{47}$$

so the optimal $d_k$ is obtained by a least-squares solution as follows:

$$d_k=\min\left(1,-\frac{(\mathbf{y}_k-\mathbf{P}\boldsymbol{\alpha}_k-\mathbf{n}_k)^\top(\mathbf{P}\boldsymbol{\alpha}_k-\mathbf{P}\boldsymbol{\alpha}_k\odot\mathbf{z}_k)}{\|\mathbf{P}\boldsymbol{\alpha}_k-\mathbf{P}\boldsymbol{\alpha}_k\odot\mathbf{z}_k\|^2}\right). \tag{48}$$

### F. IMPLEMENTATION GUIDELINES

The unified cost function of ESSEAE and NESSEAE in (10) introduced four hyperparameters $(N,\bar{\mu},\lambda,\rho)$. These hyperparameters impact the unmixing process by controlling the model order, the weight on the abundances entropy, the regularization of sparse noise, and the similarity between end-members, respectively. Their interpretation remains consistent with the original formulations of EBEAE and NEBEAE [22], [31].

With respect to the convergence properties of the iterative schemes, the optimization problems in (13), (17), (21), and (47) are convex and allow closed-form solutions in (16), (20), (34), and (48), respectively, except for NESSEAE, where a gradient descent is applied in (41) for the end-members estimation. As a consequence, within the CCDO iteration, convergence is anticipated, and at the $l$-th step, the global estimation error is computed by $J^l=\|\mathbf{Y}-\hat{\mathbf{Y}}^l\|_F$, such that:

$$\hat{\mathbf{Y}}^l=\begin{cases}\mathbf{P}^l\mathbf{A}^l+\mathbf{N}^l, & \text{(LMM)}\\ \boldsymbol{\Omega}^l\odot(\mathbf{P}^l\mathbf{A}^l)+\mathbf{D}^l\odot(\mathbf{P}^l\mathbf{A}^l)\odot\mathbf{Z}+\mathbf{N}^l, & \text{(MMM)}\end{cases} \tag{49}$$

where

$$\boldsymbol{\Omega}^l=\mathbf{1}_{L\times K}-\mathbf{D}^l\in\mathbb{R}^{L\times K}, \tag{50}$$

$$\mathbf{D}^l=[d_1^l\mathbf{1}_L\ \cdots\ d_K^l\mathbf{1}_L]\in\mathbb{R}^{L\times K}, \tag{51}$$

$$\mathbf{A}^l=[\boldsymbol{\alpha}_1^l\ \cdots\ \boldsymbol{\alpha}_K^l]\in\mathbb{R}^{N\times K}. \tag{52}$$

With these definitions, we propose the convergence conditions:

$$\frac{|J^l-J^{l+1}|}{J^l}<\epsilon\quad\vee\quad l\geq l_{max}, \tag{53}$$

where $\epsilon>0$ is a minimum improvement threshold, and $l_{max}$ the maximum iterations.

As an initialization step to ESSEAE and NESSEAE, an initial approximation for the end-members matrix $\mathbf{P}^0$ must be fully known. As assumed in our formulation, $\mathbf{P}_F$ is provided by the user, while there are two options to initialize $\mathbf{P}_U$. The first option involves the user proposing these $U$ remaining end-members. The second option is to obtain them through automatic end-member extraction methods, such as vertex component analysis (VCA) [34] or N-FINDR [35]. Our proposal accounts for the latter scenario, where the estimation of $\mathbf{P}_U$ is performed by estimating $N$ end-members. Then, using the spectral angle mapper (SAM) metric, the $U$ end-members with the largest distances to the columns in $\mathbf{P}_F$ are selected, aiming to differentiate spectra between the fixed and unknown components. Finally, an important implementation remark is related to the solutions in (13) and (48), since they are solved by each spatial point $k\in\mathcal{K}$, so their computation could be parallelized for a reduced processing time. The unified algorithm for ESSEAE and NESSEAE is described in Algorithm 1, and a block diagram description is illustrated in Fig. 2.

## III. VALIDATION METHODOLOGY

The validation stage of ESSEAE and NESSEAE considered synthetic and real-world datasets of HS images (breast histological sample and Urban dataset). For the synthetic and Urban datasets, we will have available ground-truths of end-members and their abundances, but for the breast histological sample, this information is not available. Moreover, according to the nature of these real-world datasets, either ESSEAE or NESSEAE could be better suited for spectral unmixing. Consequently, we introduce diverse scenarios of

$$\tilde{\mathrm{J}}_{MMM}=\frac{1}{2K}\sum_{k\in\mathcal{K}}\frac{\|\mathbf{v}_k^l\|^2-2(\mathbf{v}_k^l)^\top\mathbf{M}_k^l(\mathbf{P}_U^l-\gamma^l\boldsymbol{\Gamma}^l)\boldsymbol{\alpha}_{U,k}^l+(\boldsymbol{\alpha}_{U,k}^l)^\top(\mathbf{P}_U^l-\gamma^l\boldsymbol{\Gamma}^l)^\top(\mathbf{M}_k^l)^\top\mathbf{M}_k^l(\mathbf{P}_U^l-\gamma^l\boldsymbol{\Gamma}^l)\boldsymbol{\alpha}_{U,k}^l}{\|\mathbf{y}_k\|^2}+\frac{\rho}{2\vartheta}\left\{\mathrm{Tr}\left((\mathbf{P}_U^l-\gamma^l\boldsymbol{\Gamma}^l)\boldsymbol{\Theta}_1\mathbf{P}_F^\top\right)+\mathrm{Tr}\left((\mathbf{P}_U^l-\gamma^l\boldsymbol{\Gamma}^l)\boldsymbol{\Theta}_2(\mathbf{P}_U^l-\gamma^l\boldsymbol{\Gamma}^l)^\top\right)\right\} \tag{43}$$

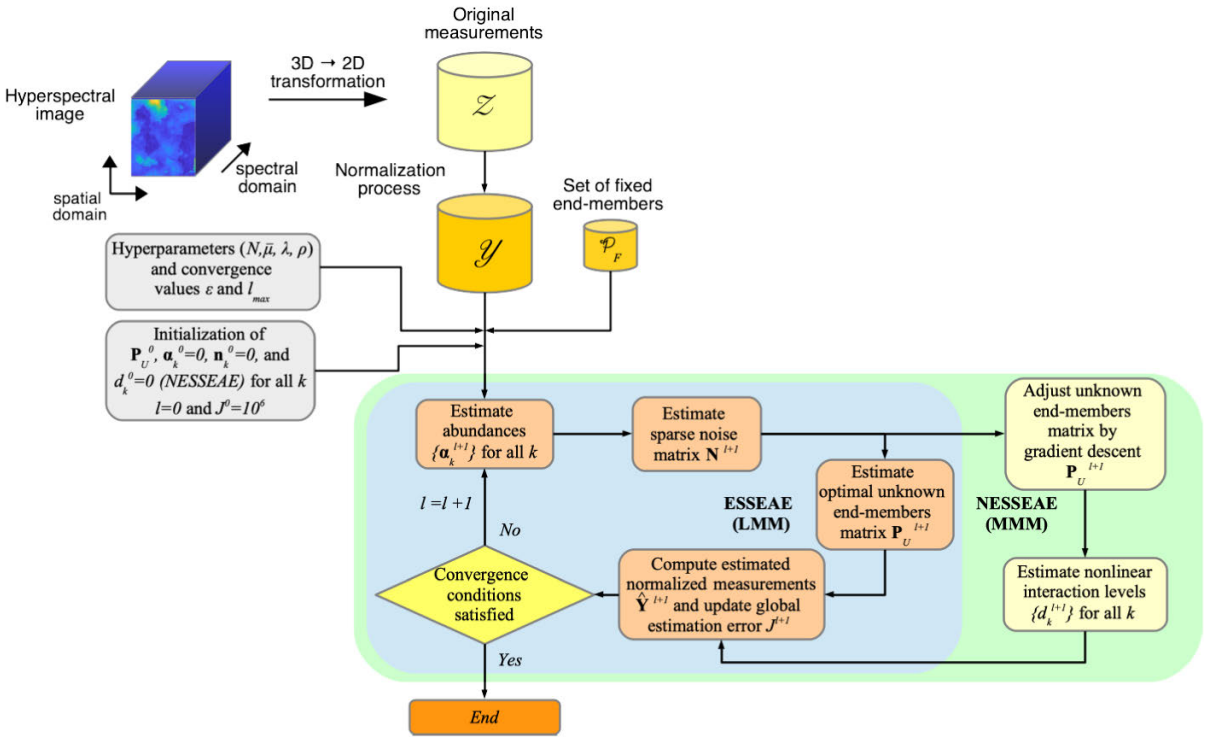


**FIGURE 2.** Block diagram of the proposed implementations of spectral unmixing: (i) ESSEAE based on a LMM, and (ii) NESSEAE based on a MMM.

**Algorithm 1** ESSEAE and NESSEAE Methodologies

**Require:** Set of original measurements $\mathcal{Z}$, hyperparameters $(N, \bar{\mu}, \lambda, \rho)$, set of fixed end-members $\mathcal{P}_F$, user propose $\mathbf{P}_U^0$ or an initialization method, and convergence parameters $\epsilon$ and $l_{max}$.

**Ensure:** unknown end-members matrix $\mathbf{P}_U$, abundances matrix $\mathbf{A} = [\mathbf{A}_F \quad \mathbf{A}_U]$ for fixed and unknown end-members, sparse noise matrix $\mathbf{N}$, estimated scaled measurements $\hat{\mathbf{Y}}$, and for NESSEAE, $\{d_k\}$ nonlinear interaction levels.

1: Normalize measurements set $\mathcal{Z}$ to obtain $\mathcal{Y}$.
2: Set $l = 0, J^0 = 10^6$, and assign abundances, sparse noise components, and for NESSEAE, nonlinear interaction levels to zero, i.e. $\boldsymbol{\alpha}_k^0 = \mathbf{0}$, $\mathbf{n}_k^0 = \mathbf{0}$, and $d_k^0 = 0\ \forall k \in \mathcal{K}$.
3: **while** Convergence condition in (53) is not satisfied. **do**
4: Update abundances $\boldsymbol{\alpha}_k^{l+1}$ by (16) $\forall k \in \mathcal{K}$.
5: Update $\mathbf{N}^{l+1}$ by (20).
6: For ESSEAE, update $\mathbf{P}_U^{l+1}$ by (34), and for NESSEAE, by the gradient descent rule in (41).
7: For NESSEAE, update $d_k^{l+1}$ by (48).
8: Compute $\hat{\mathbf{Y}}^{l+1}$ by (49), update $J^{l+1}$ and $l \leftarrow l + 1$.
9: **end while**

SSA schemes, and fixed and unknown end-members in our comprehensive validation stage, as shown in Table 1. As no previous methodologies in the state-of-the-art have addressed the SSA by simultaneous estimations of unknown end-members and overall abundances, as in our proposal, the performance results are compared with the supervised and unsupervised versions of the LMM and MMM methodologies, i.e. EBEAE and NEBEAE [22], [31] as performance references with the same hyperparameters of ESSEAE and NESSEAE. All validation schemes were implemented in Matlab, and scripts and HS datasets are available in: https://github.com/Nicothe4th/ESSEAE-NESSEAE. The computational times were evaluated in a Macbook Pro with chip Apple M3 Pro (11 cores), GPU (14 cores) and 18 GB of RAM, where the solutions (13) and (48) were parallelized by the parallel programming toolbox of Matlab [36].

### A. PERFORMANCE METRICS

To evaluate each algorithm, the following error metrics were adopted with respect to the ground-truth of measurements $E_Z$, end-members $E_p$ and $E_{SAM}$, and abundances $E_a$:

$$E_Z = \frac{\|\mathbf{Z} - \hat{\mathbf{Z}}\|_F}{\|\mathbf{Z}\|_F}, \tag{54}$$

$$E_p = \sum_{\forall \mathbf{p} \in \mathcal{P}} \min_{\forall \hat{\mathbf{p}} \in \hat{\mathcal{P}}} \frac{\|\hat{\mathbf{p}} - \mathbf{p}\|}{\|\mathbf{p}\|}, \tag{55}$$

$$E_{SAM} = \sum_{\forall \mathbf{p} \in \mathcal{P}} \min_{\forall \hat{\mathbf{p}} \in \hat{\mathcal{P}}} \arccos\left(\frac{\mathbf{p}^\top \hat{\mathbf{p}}}{\|\mathbf{p}\|\|\hat{\mathbf{p}}\|}\right), \tag{56}$$

$$E_a = \sum_{\forall \mathbf{a} \in \mathcal{A}} \min_{\forall \hat{\mathbf{a}} \in \hat{\mathcal{A}}} \frac{\|\hat{\mathbf{a}} - \mathbf{a}\|}{\|\mathbf{a}\|}, \tag{57}$$

**TABLE 1. Testing scenarios for fixed and unknown end-members during the validation stage and different datasets.**

| Dataset | Ground-truth | Spectral Unmixing Technique | End-members Fixed ($F$) | End-members Unknown ($U$) | Selection of Fixed End-members |
|---|---|---|---|---|---|
| Synthetic | Yes | Supervised | 4 | 0 | – |
| | | SSA | 3 | 1 | Randomly |
| | | SSA | 2 | 2 | Randomly |
| | | SSA | 1 | 3 | Randomly |
| | | Unsupervised | 0 | 4 | – |
| Breast Histological Sample | No | Supervised | 2 | 0 | – |
| | | SSA | 2 | 1 | Unchanged |
| | | SSA | 2 | 2 | Unchanged |
| | | SSA | 2 | 3 | Unchanged |
| | | Unsupervised | 0 | 4 | - |
| Urban | Yes | Supervised | 4 | 0 | – |
| | | SSA | 2 | 2 | Randomly |
| | | Unsupervised | 0 | 4 | – |

where $\hat{\mathbf{Z}} = [\hat{\mathbf{z}}_1, \ldots, \hat{\mathbf{z}}_K] \in \mathbb{R}^{L\times K}$ denotes the matrix of estimated measurements, and $\mathcal{A}$ refers to the set of ground-truth abundances (rows of matrix $\mathbf{A}$), and its estimation as $\hat{\mathcal{A}}$. Finally, $\hat{\mathcal{P}}$ denotes the set of estimated end-members. All error metrics $(E_Z, E_p, E_{SAM}, E_a)$ were normalized to avoid units, and they represent how closely the estimates resemble the ground-truths of each dataset. In the case of $E_Z$, the whole matrix of measurements $\mathbf{Z}$ is compared with its reconstruction $\hat{\mathbf{Z}}$ by spectral unmixing. Meanwhile, since the order of the estimated end-members by ESSEAE and NESSEAE could not match the ground-truths, and consequently, of the resulting abundance maps, we provided metrics for end-members and abundances, which are independent of the ordering in (55), (56) and (57). Thus, $E_p$ and $E_a$ are related to accumulated percentage errors in end-members and abundances estimations, respectively, and $E_{SAM}$ to the accumulated SAM between ground-truth and estimated end-members.

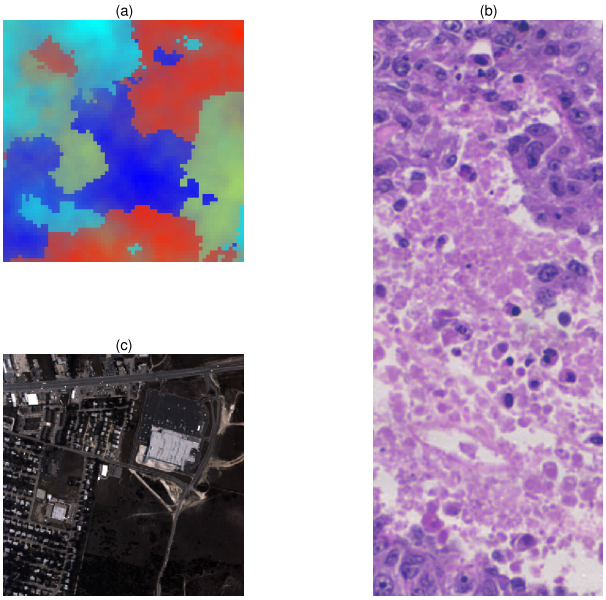


**FIGURE 3. RGB representations of the HS images used in the validation methodology: (a) Synthetic; (b) Breast histological sample; and (c) Urban dataset.**

### B. HS DATASETS AND VALIDATION PROCESS

#### 1) SYNTHETIC DATASET OF BIOLOGICAL TISSUE

The first validation stage for ESSEAE and NESSEAE considered a synthetic dataset emulating the absorption properties of biological tissue (HS image), whose spectral range was defined in the visible region (450 to 700 nm) with $64 \times 64$ pixels and 281 spectral bands (i.e. spectral resolution of 0.89 nm). The biological tissue contains four end-members ($N = 4$): oxygenated and deoxygenated hemoglobin ($HbO_2$ and $Hb$, respectively), Fat, and Water [37]. The abundance maps were generated using the HYperspectral Data Retrieval and Analysis (HYDRA) toolbox, employing a spherical Gaussian pattern with $N$=4 components [38]. Figure 3(a) illustrates the RGB representation of the ground-truth synthetic HS image. For the evaluation of NESSEAE, the nonlinear interaction levels $\{d_k\}$ followed a Gaussian distribution with a mean of 0.3 and a standard deviation of 0.1.

A Monte Carlo evaluation with 50 noise realizations was carried out to assess the robustness of the estimations by ESSEAE and NESSEAE, where two types of noise were added: Gaussian and sparse uniformly distributed (SUD) [31]. Gaussian noise was quantified by a signal-to-noise ratio (SNR) at values of 40, 35, and 30 dB, and SUD noise by density levels of 0.005, 0.0075, and 0.01 with a maximum value of 20% of the peak spectral response in the noiseless dataset. In addition, we varied the number of unknown end-members from zero to four ($U \in \{0, 1, 2, 3, 4\}$), i.e. we covered from a supervised case ($U = 0$) to an unsupervised estimation ($U = 4$), as described in Table 1. In each Monte Carlo evaluation, for the semi-supervised cases $U \in \{1, 2, 3\}$, the fixed end-members were randomly selected from the ground-truth, while the rest were considered unknown. The hyperparameters and convergence thresholds in ESSEAE and NESSEAE during the synthetic evaluation are described in Table 2. According to [22] and [31], the value of $\bar{\mu}$ was selected to add some robustness in the

abundances estimation due to Gaussian noise, and $\rho$ as an intermediate value to balance the expected morphology of end-members (similar *vs* quite different). Meanwhile, the value of $\lambda$ adds robustness to sparse noise in the estimations of end-members and abundances. In all cases, the initialization of the end-members matrix was carried out by VCA [34], which produced slightly better results than N-FINDR in our implementations [35].

#### 2) BREAST HISTOLOGICAL SAMPLE

In the second validation stage, a visible near-infrared (VNIR) image of a breast histological section in transmittance mode was used, which was stained with Eosin (E) and Hematoxylin (H), and cut at a thickness of 4-5 $\mu m$, as described in [39]. The spectral range of the VNIR dataset was from 450 to 900 nm, with a resolution of 2.8 nm, yielding HS images of 1004 $\times$ 400 pixels across 128 spectral bands after pre-processing [39]. A mask was used to discard non-tissue areas illuminated solely by the microscope light (blank spaces), i.e. the region of interest (ROI) in the image is where the tissue is present. Figure 3(b) presents a synthetic RGB image of the breast histological sample generated from the HS cube. Since in this VNIR dataset, no high-order optical interactions are expected due to the controlled scenario in the microscope, only ESSEAE was evaluated. The objective of the unmixing scheme is to separate the spectral contributions of the stains from the cellular structures.

The hyperparameters in ESSEAE were manually fine-tuned to enhance unmixing performance: $\bar{\mu} = 0.2$, $\rho = 0.01$, and $\lambda = 0.1$ with the same convergence conditions of the synthetic evaluation (see Table 2). The spectral signatures of Hematoxylin and Eosin were assumed as the fixed end-members ($F = 2$), see Table 1. Meanwhile, one, two and three end-members were considered as unknown in the analysis, i.e. ($U \in \{1, 2, 3\}$), and were initialized by N-FINDR [35]. The supervised scenario ($U = 0$), where only the stains of H&E were used as fixed en-members, was also analyzed. So, in this validation stage, the LMM order was varied in the set $N \in \{2, 3, 4, 5\}$. For comparison purposes, an unsupervised unmixing by EBEAE with four unknown end-members ($F = 0$ & $U = 4$) was implemented in this validation stage with an initialization by N-FINDR [35].

#### 3) URBAN DATASET

Finally, the Urban dataset is a widely recognized benchmark in the literature of remote sensing, and it was obtained by advanced imaging sensors in an urban environment [10]. As a result, the HS dataset presents high-order optical effects that could be approximated by a MMM, so the unmixing process is more suitable for NESSEAE. This HS dataset has a spatial resolution of 307 $\times$ 307 pixels with 162 spectral bands that cover the wavelength range from 400 to 2500 nm. Figure 3(c) shows a synthetic RGB image of the Urban dataset. There are three versions of ground-truths with four, five and six end-members. For this validation stage, we consider the case of four end-members with their respective abundances as a reference, i.e. $N = 4$. The physical interpretation of the end-members is as follows:1-*Asphalt Road*, 2-*Grass*, 3-*Tree*, and 4-*Roof*.

The hyperparameters of NESSEAE were slightly adjusted from the synthetic scenario (see Table 2) to optimize the estimation process for the Urban dataset: $\bar{\mu} = 0.01$, $\rho = 1.0$ and $\lambda = 0.1$. The results with the initialization of the end-members matrix by N-FINDR or VCA were indistinct in both cases. Eight scenarios were evaluated for the Urban dataset. Six scenarios used a fixed set of end-members ($F = 2$), while exploring all possible pairings of two unknown endmembers ($U = 2$) 1 & 2, 1 & 3, 1 & 4, 2 & 3, 2 & 4, and 3 & 4 (see Table 1). The remaining two cases were supervised and unsupervised conditions ($F = 4$ & $U = 0$, and $F = 0$ & $U = 4$, respectively), as performance references.

## IV. RESULTS AND DISCUSSION

### A. SYNTHETIC EVALUATION

#### 1) ESSEAE RESULTS

For ESSEAE (LMM case), the Monte Carlos results are presented as boxplots in Fig. 4 for the synthetic datasets. The measurement error $E_Z$ showed a particular trend, where the most significant change was related to the noise contribution, and barely constant with respect to the number of unknown end-members. However, there was a smaller error for the unsupervised approach, i.e. $U = 4$. This superior performance can be attributed to the initialization process of the end-members by VCA [34]. So, the initial end-members were adapted to the induced distortion by the two types of noise sources in the synthetic datasets, and as a consequence, the overall measurement error $E_Z$ was reduced, compared to the semi-supervised and supervised conditions ($U \in \{0, 1, 2, 3\}$). As expected, in $E_a$, $E_p$, and $E_{SAM}$, errors increased constantly as the number of unknown end-members also increased. However, the medians of $E_a$, $E_p$ and $E_{SAM}$ were always lower than 0.13, 0.08 and 0.06, respectively, to highlight high precision despite added noise. Furthermore, in general, the medians of the errors did not show significant changes with the increments in noise contributions. With respect to computational time, as expected, the unsupervised methodology ($F = 0$ & $U = 4$) required the highest one (roughly twice of the semi-supervised scenarios). The semi-supervised cases ($U \in \{1, 2, 3\}$) presented roughly flat responses in the medians, with values always lower than 0.3 seconds. In this case, the supervised methodology ($F = 4$ & $U = 0$) achieved just higher computational time (medians between 0.3 and 0.35 seconds) than the semi-supervised conditions. Finally, as the noise was raised, there was roughly no effect in the computational time. For a qualitative evaluation, Figs. 5(a) and 5(b) present the ground-truths end-members and their abundances maps, respectively, in the synthetic datasets. Meanwhile, for testing scenario $F = 1$ & $U = 3$, Figs. 5(c) and 5(d) illustrate an example of the resulting estimations

**TABLE 2. Hyperparameters, convergence thresholds and initialization of end-members mntrix of ESSEAE and/or NESSEAE during the validation methodology.**

| Parameter | Synthetic Dataset | Breast Histological Sample | Urban Dataset |
|---|---|---|---|
| $\bar{\mu}$ (abundances entropy) | 0.1 | 0.2 | 0.01 |
| $\rho$ (end-members similarity) | 0.1 | 0.01 | 1.0 |
| $\lambda$ (sparse noise regularization) | 0.1 | 0.1 | 0.1 |
| $\epsilon$ (minimum improvement threshold) | 0.001 | 0.001 | 0.001 |
| $l_{max}$ (maximum number of iterations) | 20 | 20 | 20 |
| Initial unknown end-members $\mathbf{P}_U^0$ | VCA | N-FINDR | N-FINDR / VCA |

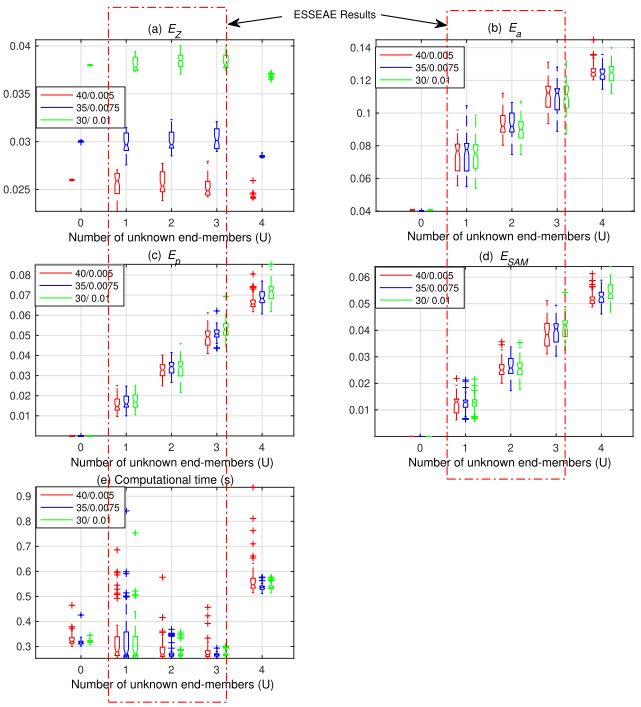


**FIGURE 4. Monte carlos results of ESSEAE at different number of unknown end-members and noise levels (SNR dB/SUD density): (a) Measurement error $E_Z$; (b) Abundance error $E_a$; (c) End-member error $E_p$; (d) End-member SAM metric $E_{SAM}$; and (e) computational time.**

for end-members and abundance maps, respectively, under the highest noise condition (30 dB of Gaussian noise and 0.01 of SUD density). As a result, comparing with the ground-truths in Figs. 5(a) and 5(b), we can observe precise reconstructions of end-members and abundance maps by ESSEAE.

It is important to highlight the potential of the SSA approach for practical applications. The examples shown in Figs. 5(b) and 5(c) illustrate a scenario where prior knowledge of the biological sample includes only one known end-member (Water). Despite this limited prior information, the SSA method can successfully extract additional end-members, and analyzing these can help to identify other biochemical components present in the sample. For instance, based on the absorption peaks observed in Figs. 5(b) and 5(c), we can infer that "Unknown-1" corresponds to *Hb*, "Unknown-2" to $HbO_2$, and "Unknown-3" to Fat. With this insight, we can conclude that the biological sample consists of four identified components: $H_b$, $HbO_2$, Fat and Water. We can then incorporate these end-members as fixed references and reapply the SSA method, allowing us to uncover any additional potential components that may be present in the biological sample depicted in the image.

### 2) NESSEAE RESULTS

Similarly, for NESSEAE (MMM case), the boxplot results are now presented in Fig. 6 for the synthetic datasets. The trends for $\{E_Z, E_a, E_p, E_{SAM}\}$ resemble the results for ESSEAE in Fig. 4. But now, the medians of $E_a$, $E_p$ and $E_{SAM}$ were slightly improved and always lower than 0.12, 0.06 and 0.05, respectively, showing high precision despite the added noise (see Fig. 6). Furthermore, the computational time increased with respect to the results for ESSEAE, which was expected, since there is no closed-form solution for the unknown end-members matrix [31]; so for the semi-supervised and unsupervised cases ($U \in \{1, 2, 3, 4\}$), the median of the computational time was less than 2.5 seconds. In fact, the shortest computational time was achieved by the supervised case ($F = 4$ & $U = 0$). In addition, as the noise raised, the computational time was not affected. Finally, to evaluate qualitatively testing scenario $F = 1$ & $U = 3$ for NESSEAE, Figs. 5(e) and 5(f) show an example of the estimated end-members and abundance maps for the highest noise condition (30 dB of Gaussian noise and 0.01 of SUD density). Consequently, a direct comparison with the ground-truths in Figs. 5(a) and 5(b) shows once more accurate reconstructions of end-members and abundance maps by NESSEAE.

### 3) NUMERICAL CONVERGENCE

Finally, to evaluate the convergence of the proposed methodologies, ESSEAE and NESSEAE, the stopping criterion in (53) was modified in Algorithm 1, just to consider the maximum number of iterations. This scenario allowed for the analysis of the global estimation error $J^i$ at each iteration $i$ for visual verification of its convergence. For this last experiment, the number of unknown end-members was varied from one to three ($U \in \{1, 2, 3\}$), and the noise scenario was set to 30 dB of Gaussian noise and a 0.01 SUD density, i.e. highest noise condition. The results in Fig. 7 show that the convergence of both methodologies is ensured despite the number of unknown end-members, where in general, ESSEAE and NESSEAE reached a fast convergence in approximately less than five iterations.

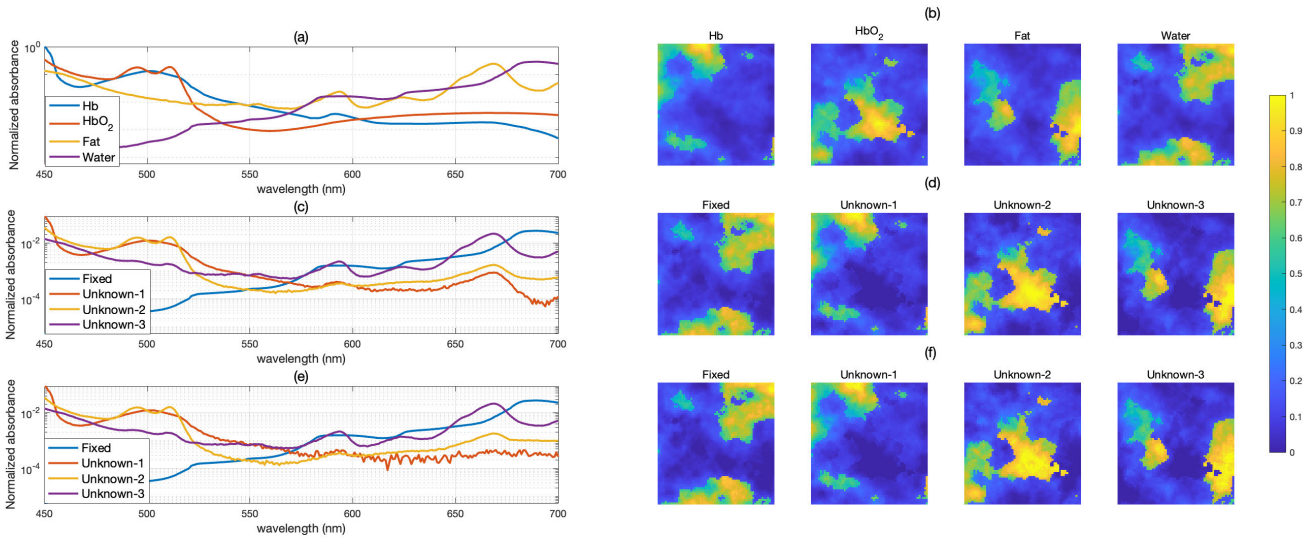


**FIGURE 5.** ESSEAE and NESSEAE evaluation using synthetic datasets: (a) Ground-truth of end-members; (b) Ground-truth of abundance maps; (c) End-members estimation using ESSEAE ($F = 1$ & $U = 3$) of one realization for 30 dB and 0.01 SUD density; (d) Corresponding ESSEAE abundance maps; (e) End-members estimation using NESSEAE ($F = 1$ & $U = 3$) of one realization for 30 dB and 0.01 SUD density; (e) Corresponding NESSEAE abundance maps.

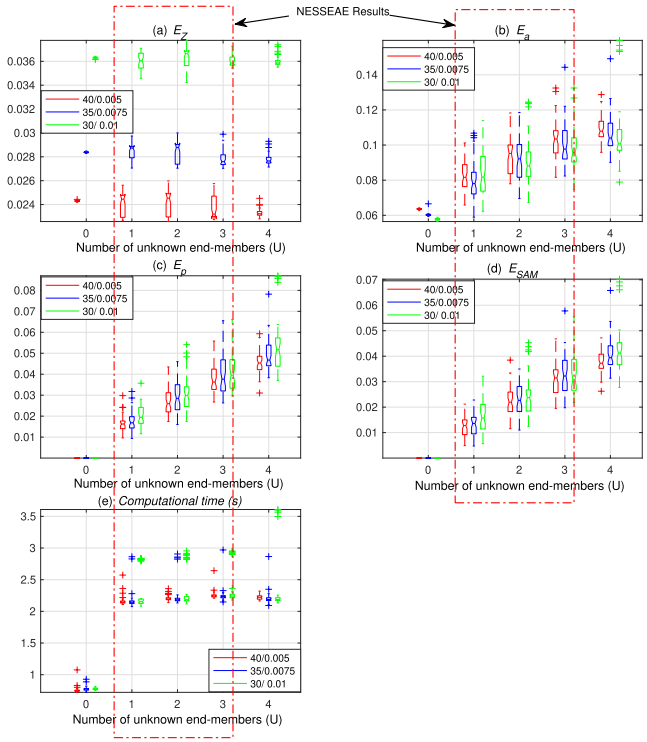


**FIGURE 6.** Monte Carlos results of NESSEAE at different number of unknown end-members and noise levels (SNR dB/SUD density): (a) Measurement error $E_Z$; (b) Abundance error $E_a$; (c) End-member error $E_p$; (d) End-member SAM metric $E_{SAM}$; and (e) computational time.

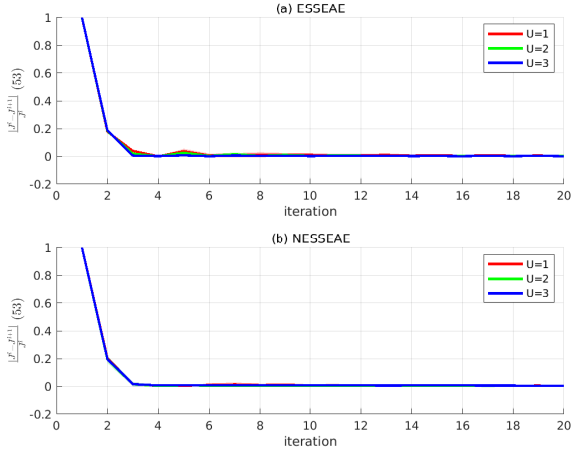


**FIGURE 7.** Evaluation with synthetic datasets (30 dB and 0.01 SUD density, and $U \in \{1, 2, 3\}$): Increments in global estimation error for convergence analysis (a) ESSEAE, and (b) NESSEAE.

**TABLE 3.** Evaluation of breast histological sample: Measurement error and computational time for $U \in \{0, 1, 2, 3, 4\}$. (Highlighted with a bold font the best performance).

| Methodology | End-members Fixed ($F$) | End-members Unknown ($U$) | Measurements error ($E_z$) | Computational time (seconds) |
|---|---|---|---|---|
| EBEAE-Supervised | 2 | 0 | 0.1650 | **1.51** |
| ESSEAE | 2 | 1 | 0.0721 | 15.38 |
| ESSEAE | 2 | 2 | 0.0529 | 28.07 |
| ESSEAE | 2 | 3 | **0.0488** | 31.91 |
| EBEAE-Unsupervised | 0 | 4 | 0.0531 | 15.56 |

### B. REAL-WORLD EVALUATION

#### 1) ESSEAE RESULTS

In this section, we describe qualitative and quantitative results of ESSEAE for the breast histological sample and testing cases in Table 1. For the first testing scenario, i.e. supervised approach ($F = 2$ & $U = 0$), Figs. 8(a) and 8(b) present the spectral response of the fixed end-members H&E, and their corresponding abundances map, respectively. These end-members present clear differences in their spectral responses in the interval 500 to 700 nm, but the

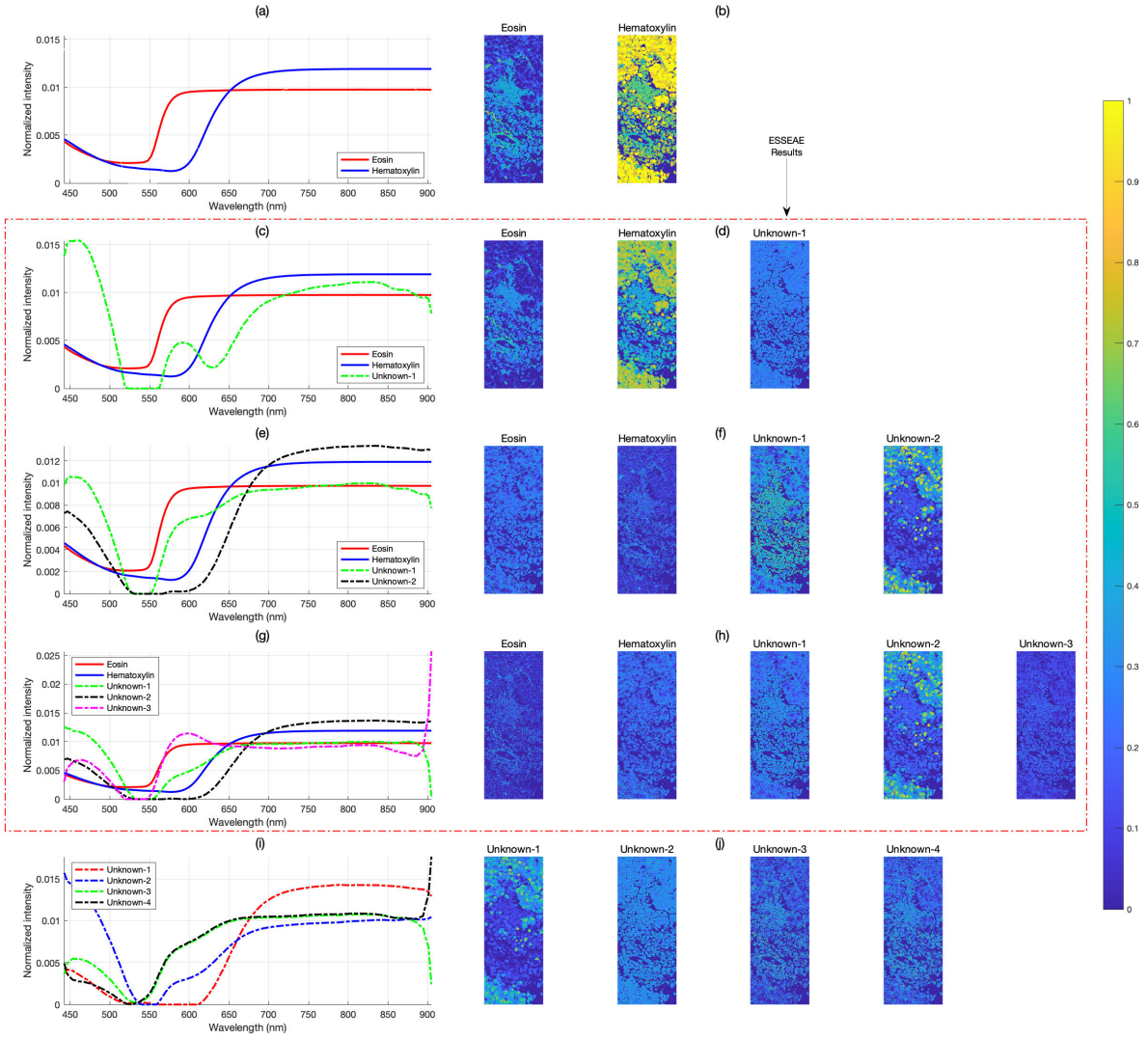


**FIGURE 8.** ESSEAE evaluation results of breast histological sample: Supervised unmixing results ($F = 2$ & $U = 0$) (a) end-members and (b) abundance maps; SSA results ($F = 2$ & $U = 1$) (c) end-members and (d) abundances maps; SSA results ($F = 2$ & $U = 2$) (e) end-members and (f) abundances maps; SSA results ($F = 2$ & $U = 3$) (g) end-members and (h) abundance maps; Unsupervised estimation results ($F = 0$ & $U = 4$) (i) end-members and (j) abundance maps.

resulting abundances maps do not highlight a clear distinction in the cell structures, since the hematoxylin end-member captures most of the abundance information. For the second scenario $F = 2$ & $U = 1$, Fig. 8(c) shows that end-member "Unknown-1" presents a completely different morphology to H&E, where its peak response is achieved around 450 nm and presents a region of a very small gain between 500 and 600 nm. With respect to the resulting abundance maps in Fig. 8(d), once more the hematoxylin end-member gathered most of the abundance information, so resulting in maps with less contrast compared to the RGB image (see Fig. 3(b)). For $F = 2$ & $U = 2$, Fig. 8(e) illustrates that the resulting unknown end-members seem to be paired, since the morphology of "Unknown-1" is similar to eosin above 550 nm, and "Unknown-2" to hematoxylin in the same range. The abundance maps in Fig. 8(f) highlight that the cell nuclei can be now distinguished by end-member "Unknown-2". In this way, the spectral information between 450 and 550 nm of "Unknown-1" and "Unknown-2" allowed the segmentation process. For $F = 2$ & $U = 3$, Fig. 8(g) shows that end-member "Unknown-3" is similar to eosin in the range 550 to 850 nm, and "Unknown-1" to hematoxylin in the same interval. Meanwhile, "Unknown-2" is characterized by a small gain roughly in the range 520 to 620 nm, and is practically identical to "Unknown-1" below 520 nm. So, we observe some redundancy in the end-members' spectral responses for this scenario, as will be corroborated by the analysis of the abundance maps. Figure 8(h) presents the five abundance maps for this testing case, where we confirm the redundancy. Once more, "Unknown-2" described the

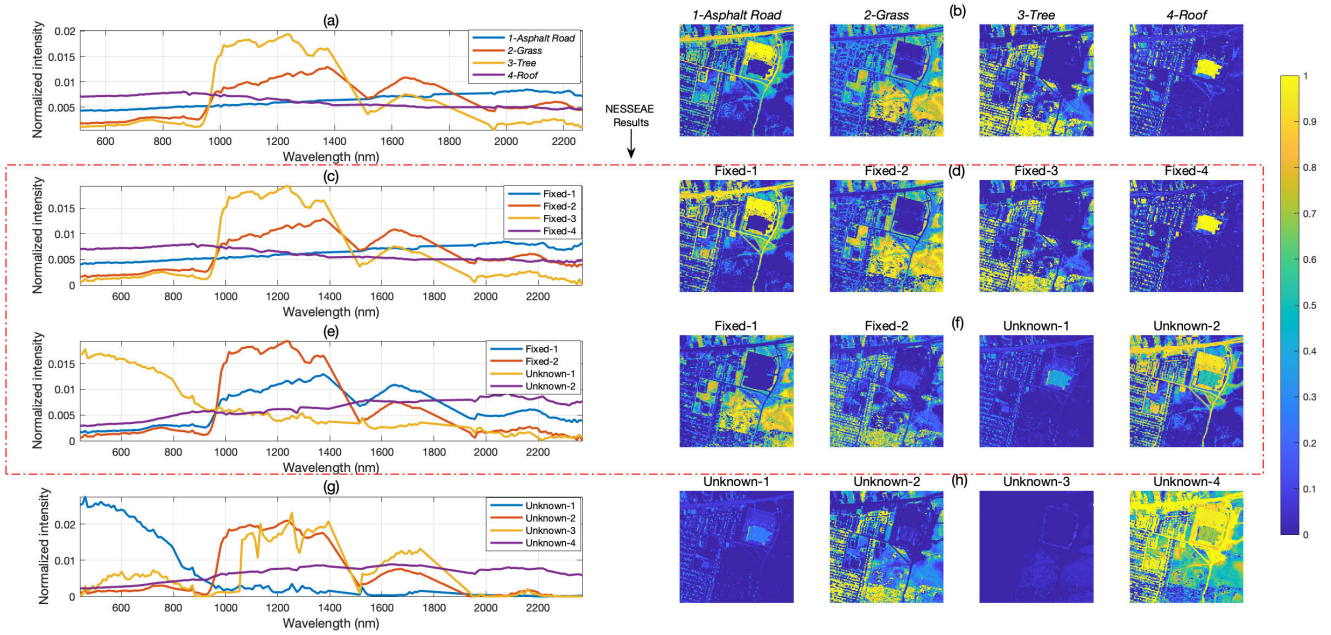


**FIGURE 9.** NESSEAE evaluation results or Urban dataset: (a) Ground-truths of end-members, and of (b) abundance maps; Supervised estimation results ($F = 4$ & $U = 0$) (c) end-members and (d) abundance maps; NESSEAE results ($F = 2$ & $U = 2$) where end-members 2 and 3 are fixed (i.e. *Grass* and *Tree*) (e) estimated end-members and (f) abundance maps; Unsupervised estimation results ($F = 0$ & $U = 4$) (g) end-members and (h) abundance maps.

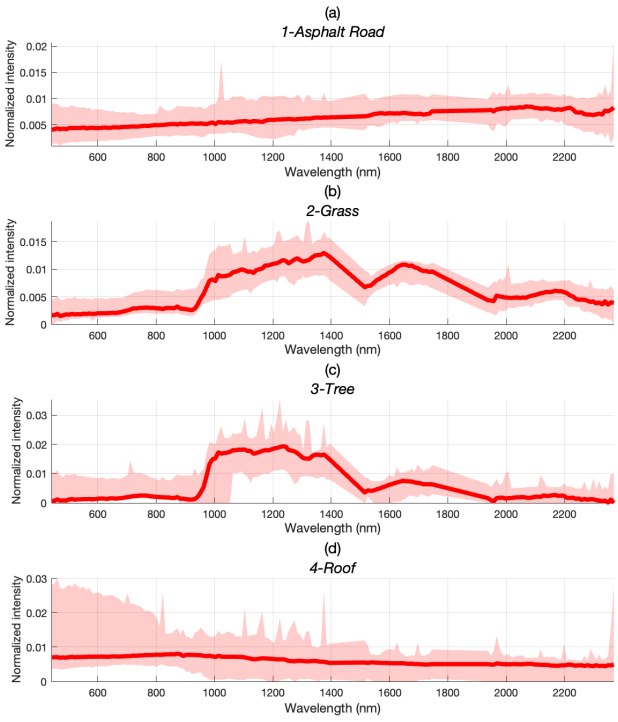


**FIGURE 10.** Evaluation of Urban dataset: Ground-truth end-members (solid traces) and min-max variability (shaded area) in spectral response (a) 1-*Asphalt Road*; (b) 2-*Grass*; (c) 3-*Tree*; and (d) 4-*Roof*.

cell nuclei, as in the previous scenario ($F = 2$ & $U = 2$), but "Unknown-3" did not show any relevance and the spatial contribution of the eosin end-member almost vanished. Finally, for the unsupervised scenario ($F = 0$ & $U = 4$) in Fig. 8(i), there is some redundancy in "Unknown-3" and "Unknown-4" in the interval 540 to 850 nm, and between "Unknown-1" and "Unknown-4" inside 450 to 540 nm. So, the only end-member with completely different spectral response is "Unknown-2". The resulting abundances are shown in Fig. 8(j), where the more distinctive map is related to "Unknown-1", while the rest does not highlight clear cell structures. Hence, our qualitative evaluation of the testing cases in Table 1 revealed that the clearest segmentation of cell structures in the histological sample was achieved with $F = 2$ & $U = 2$.

Table 3 introduces the quantitative results for this real-world evaluation. Since for this dataset there are no ground-truths, just the measurement error $E_Z$ and computational time were obtained. Our results showed that the measurement error $E_Z$ in the supervised approach ($F = 2$ & $U = 0$) is the highest among all scenarios, more than twice as large compared to the case of adding one unknown end-member ($U = 1$). Furthermore, as the number of unknown end-members increased in Table 3, the measurement error $E_z$ decreased, while the computational time increased. So, the lowest measurement error $E_Z$ was achieved with $F = 2$ & $U = 3$. However, the error change from $U = 2$ to $U = 3$ was small, compared to the previous two cases $U = 0$ and $U = 1$. With respect to computational time, there is a substantial increase with respect to the supervised approach ($F = 2$ & $U = 0$), which is compensated by the large improvement in $E_Z$. Meanwhile, for the unsupervised scenario ($F = 0$ & $U = 4$), the measurement error $E_Z$ was slightly higher to the case $F = 2$ & $U = 2$, but with a lower computational time. In summary, by considering the

**TABLE 4. Evaluation of Urban dataset: Estimated errors for different pairs of fixed end-members (1-*Asphalt Road*; 2-*Grass*; 3-*Tree*; and 4-*Roof*) (Highlighted with a bold font the best performance).**

| Metric | NEBEAE -Supervised ($F=4$ & $U=0$) | NESSEAE ($F=2$ & $U=2$) Fixed End-members 1 & 2 | 1 & 3 | 1 & 4 | 2 & 3 | 2 & 4 | 3 & 4 | NEBEAE -Unsupervised ($F=0$ & $U=4$) |
|---|---|---|---|---|---|---|---|---|
| Measurement error ($E_z$) | 0.0870 | 0.0605 | **0.0580** | 0.0807 | 0.0583 | 0.0716 | 0.0681 | 0.0791 |
| Abundance error ($E_a$) | **0.2085** | 0.3996 | 0.3804 | 0.5806 | 0.3540 | 0.5749 | 0.5973 | 0.7056 |
| End-member error ($E_p$) | - | **0.1143** | 0.1343 | 0.1451 | 0.1352 | 0.1151 | 0.1953 | 0.2728 |
| End-member SAM metric ($E_{SAM}$) | - | **0.1139** | 0.1210 | 0.1336 | 0.1340 | 0.1150 | 0.1741 | 0.2653 |
| Computational time (s) | **3.3293** | 24.7535 | 27.3272 | 18.9193 | 48.1490 | 26.5509 | 26.3179 | 24.8909 |

measurement errors, computational time, and a qualitative evaluation of the end-members and abundance maps, the best trade-off in segmentation and estimation performance by ESSEAE was achieved with $F = 2$ & $U = 2$, i.e. $N = 4$. In conclusion, ESSEAE required two unknown end-members besides the fixed ones for H&E to provide the desired segmentation in this testing scenario.

### 2) NESSEAE RESULTS

This section introduces qualitative and quantitative results of NESSEAE for the testing cases in Table 1 related to Urban dataset. The ground-truths of end-members and abundance maps are illustrated in Figs. 9(a) and 9(b), respectively. For a qualitative evaluation, supervised ($F = 4$ & $U = 0$), semi-supervised ($U = 2$ & $F = 2$ with 2-*Grass* and 3-*Tree* as fixed end-members) and unsupervised ($F = 0$ & $U = 4$) cases are all illustrated in Figs. 9(c) to 9(h). Figure 9(d) shows that for the supervised case, and as expected, the abundance maps have a high resemblance to the ground-truths in Fig. 9(b). Meanwhile, for the semi-supervised case, the estimated unknown end-members in Fig. 9(e) as "Unknown-1" is associated with 4-*Roof*, while "Unknown-2" is related to 1-*Asphalt Road*. This association can be easily seen by the correspondence in the abundance maps in Figs. 9(b) and 9(f). In the morphology of the estimated end-members, "Unknown-1" exhibited the largest differences from its ground-truth in the first spectral channels. In the middle ones, instead of a smooth transition, the estimation displayed a constant noisy decay.

To provide some reasoning for this trend, we performed a data exploration step by using the abundance ground-truth maps shown in Fig. 9(b), where we selected the pixels with abundances greater than 0.6 to derive min-max intervals of variation in the spectral responses. In this way, Figs. 10(c) and (d) illustrate large variability in the first spectral channels of end-members 3-*Tree* and 4-*Roof*, respectively, as well as in the middle bands of end-members 2-*Grass* and 3-*Tree* (see Figs. 10(b) and (c)). Also, a roughly flat response in the spectral features is observed by 1-*Asphalt Road* and 4-*Roof* (see Figs. 10(a) and (d)). Consequently, the substantial differences in the estimated end-members by ESSEAE in Fig. 9(e) are attributed to the high variability in spectral response by end-member 4-*Roof*, as shown in Fig. 10(d). In contrast, the differences between 1-*Asphalt Road* and "Unknown-2" are subtler, with both showing similar value ranges, although the ground-truth presents a smoother morphology. The resulting abundance maps of ESSEAE are shown in Fig. 9(f), where the areas of high abundance for each end-member are largely preserved in both cases, although "Unknown-1" displays lower values compared to its respective ground-truth (4-*Roof* in Fig. 9(b)). Finally, the results for the unsupervised case ($F = 0$ & $U = 4$) are presented in Figs. 9(g) and 9(h), where we observe that the spectral variability illustrated in Fig. 10 misled the estimations by the unsupervised approach, as well as the lack of spectral features by 1-*Asphalt Road* and its similarity to 4-*Roof*. As a result, the resulting end-members and their abundances maps were not precise in the unsupervised case.

The quantitative results are presented in Table 4 for the Urban dataset. For the measurement error $E_Z$, our evaluation showed that in most conditions the SSA slightly outperformed both the supervised ($F = 4$ & $U = 0$) and unsupervised ($F = 0$ & $U = 4$) methods. This trend can be associated to the large variability in the spectral response with respect to the ground-truth end-members, as shown in Fig. 10. Nonetheless, the measurement estimation was always precise, since $E_Z$ was bounded between 6% and 9% in all scenarios. For abundance error $E_a$, as expected, the top performance was achieved by the supervised scheme, and the corresponding errors by NESSEAE were always lower than the unsupervised approach with NEBEAE. So, as shown in Fig. 9(h), the estimations of the abundance maps by the unsupervised approach were not accurate. In fact, high values in $E_a$ for NESSEAE were consistently achieved when end-member 4-*Roof* was fixed (i.e. 1 & 4, 2 & 4, and 3 & 4), since as illustrated in Fig. 10(d), there is a large variability in the spectral response associated with that case. Now, for the performance in end-members estimation by $E_p$ and $E_{SAM}$, all the scenarios of NESSEAE were much lower than the unsupervised approach. Finally, since in the supervised approach there is no estimation of end-members, this scheme achieved the lowest computational time (3.3 s), and for the rest, the values were in the range from 19 to 48 s. As a result, for the Urban dataset, previous knowledge by following a SSA clearly improved the estimations of end-members and their abundances with NESSEAE, but this extra knowledge did not reflect in a reduction of computational time, which could be larger than the unsupervised scheme.

## V. CONCLUSION

This paper introduced ESSEAE and NESSEAE methodologies as SSA for LMM and MMM scenarios, respectively,

designed for versatile applications in biomedical imaging and remote sensing. Both approaches leverage CCDO for their implementation, and our framework incorporated the ability to account for Gaussian and sparse noise along the spectral dimension. Since in some scenarios just partial information of the end-members is known before hand, the key innovation of this work lies in the unexplored SSA, where a subset of end-members is known, while the remaining end-members are either unknown or only poorly characterized. A comprehensive validation process was carried out across distinct scenarios: synthetic and real-world datasets. It is important to highlight the potential and relevance of the SSA perspective for practical applications in real-world scenarios, especially when there is only partial prior knowledge of the sample composition. The SSA method effectively identifies the abundances of both known and unknown materials present in a scene, producing results that are more interpretable than those by unsupervised unmixing techniques, which cannot incorporate prior information about the sample composition into the analysis. Furthermore, SSA offers greater flexibility in its outcomes compared to supervised methods, which are restricted to the end-members defined for the sample composition.

The main limitations of the proposed methodologies ESSEAE and NESSEAE occurred when attempting to estimate more end-members than the fixed number, resulting in highly similar unknown end-members and/or redundant abundance maps; or facing heavy spectral variability in the fixed end-members, affecting the reconstruction of abundance maps. For future work, our aim is to provide an automated adjustment of hyperparameters in ESSEAE and NESSEAE that will rely on the studied dataset and available ground-truths. We also plan to extend the histological evaluation to more diverse biomedical imaging scenarios, and to focus on proposing classification methodologies using deep learning. Finally, our research team is developing a toolbox in Python with our contributions in supervised, semi-supervised and unsupervised spectral unmixing approaches with LMM and MMM.

## APPENDIX

In this Appendix, we present the derivation of the end-members similarity term (*iv*) in (10) without the weight $\rho/2\vartheta$. First, we define each component in (*iv*) as:

$$\Phi_1 \triangleq \sum_{f=1}^{F}\sum_{u=F+1}^{F+U} \|\mathbf{p}_f - \mathbf{p}_u\|^2, \tag{58}$$

$$\Phi_2 \triangleq \sum_{u=F+1}^{F+U-1}\sum_{j=u+1}^{F+U} \|\mathbf{p}_u - \mathbf{p}_j\|^2. \tag{59}$$

A direct derivation of $\Phi_1$ shows that

$$\begin{aligned}\Phi_1 &= \|\mathbf{p}_1 - \mathbf{p}_{F+1}\|^2 + \cdots + \|\mathbf{p}_1 - \mathbf{p}_N\|^2 + \\ &\quad \vdots \\ &\quad + \|\mathbf{p}_F - \mathbf{p}_{F+1}\|^2 + \cdots + \|\mathbf{p}_F - \mathbf{p}_N\|^2 \\ &= (\mathbf{p}_1 - \mathbf{p}_{F+1})^\top(\mathbf{p}_1 - \mathbf{p}_{F+1}) + \cdots \\ &\qquad + (\mathbf{p}_1 - \mathbf{p}_N)^\top(\mathbf{p}_1 - \mathbf{p}_N) + \\ &\quad \vdots \\ &\quad (\mathbf{p}_F - \mathbf{p}_{F+1})^\top(\mathbf{p}_F - \mathbf{p}_{F+1}) + \cdots \\ &\qquad + (\mathbf{p}_F - \mathbf{p}_N)^\top(\mathbf{p}_F - \mathbf{p}_N) \qquad (60)\\ &= U\,\mathbf{p}_1^\top\mathbf{p}_1 - 2\mathbf{p}_1^\top\sum_{j=F+1}^{N}\mathbf{p}_j + \sum_{j=F+1}^{N}\mathbf{p}_j^\top\mathbf{p}_j + \\ &\quad \vdots \\ &\quad U\,\mathbf{p}_F^\top\mathbf{p}_F - 2\mathbf{p}_F^\top\sum_{j=F+1}^{N}\mathbf{p}_j + \sum_{j=F+1}^{N}\mathbf{p}_j^\top\mathbf{p}_j \qquad (61)\\ &= U\sum_{f=1}^{F}\mathbf{p}_f^\top\mathbf{p}_f - 2\left(\sum_{f=1}^{F}\mathbf{p}_f^\top\right)\left(\sum_{j=F+1}^{N}\mathbf{p}_j\right) + F\sum_{j=F+1}^{N}\mathbf{p}_j^\top\mathbf{p}_j \qquad (62)\\ &= U\ \mathrm{Tr}(\mathbf{P}_F\mathbf{P}_F^\top) - 2\,(\mathbf{P}_F\mathbf{1}_F)^\top\,(\mathbf{P}_U\mathbf{1}_U) + F\ \mathrm{Tr}(\mathbf{P}_U\mathbf{P}_U^\top) \qquad (63)\\ &= U\mathrm{Tr}(\mathbf{P}_F\mathbf{P}_F^\top) + F\mathrm{Tr}(\mathbf{P}_U\mathbf{P}_U^\top) + \mathrm{Tr}\left(\mathbf{P}_U[-2\mathbf{1}_U\mathbf{1}_F^\top]\mathbf{P}_F^\top\right), \qquad (64)\end{aligned}$$

since $N = F + U$. Meanwhile, for the remaining term $\boldsymbol{\Theta}_2$, we obtain

$$\begin{aligned}\Phi_2 &= \frac{1}{2}\sum_{u=F+1}^{N}\sum_{j=F+1}^{N}\|\mathbf{p}_u - \mathbf{p}_j\|^2 \qquad (65)\\ &= U\sum_{u=F+1}^{N}\|\mathbf{p}_u\|^2 - \left(\sum_{u=F+1}^{N}\mathbf{p}_u\right)^\top\left(\sum_{j=F+1}^{N}\mathbf{p}_j\right) \qquad (66)\\ &= U\ \mathrm{Tr}(\mathbf{P}_U\mathbf{P}_U^\top) - (\mathbf{P}_U\mathbf{1}_U)^\top\,(\mathbf{P}_U\mathbf{1}_U) \qquad (67)\\ &= U\ \mathrm{Tr}(\mathbf{P}_U\mathbf{P}_U^\top) - \mathrm{Tr}\left(\mathbf{P}_U\mathbf{1}_U\mathbf{1}_U^\top\mathbf{P}_U^\top\right). \qquad (68)\end{aligned}$$

Finally, by adding the resulting terms $\Phi_1$ and $\Phi_2$, we reach

$$\begin{aligned}\Phi_1 + \Phi_2 &= U\ \mathrm{Tr}(\mathbf{P}_F\mathbf{P}_F^\top) + (F+U)\ \mathrm{Tr}(\mathbf{P}_U\mathbf{P}_U^\top) \qquad (69)\\ &\quad + \mathrm{Tr}\left(\mathbf{P}_U[-2\mathbf{1}_U\mathbf{1}_F^\top]\mathbf{P}_F^\top\right) - \mathrm{Tr}\left(\mathbf{P}_U\mathbf{1}_U\mathbf{1}_U^\top\mathbf{P}_U^\top\right) \\ &= U\ \mathrm{Tr}(\mathbf{P}_F\mathbf{P}_F^\top) + \mathrm{Tr}\left(\mathbf{P}_U\boldsymbol{\Theta}_2\mathbf{P}_U^\top\right) + \mathrm{Tr}\left(\mathbf{P}_U\boldsymbol{\Theta}_1\mathbf{P}_F^\top\right), \qquad (70)\end{aligned}$$

and since the element $\mathrm{Tr}(\mathbf{P}_F\mathbf{P}_F^\top)$ is fixed during the overall estimation process in (10), we conclude that the equivalent optimization for the unknown end-members $\mathbf{P}_U$ is provided in (21).

## REFERENCES

[1] J. M. Amigo, *Hyperspectral Imaging*. Amsterdam, The Netherlands: Elsevier, 2019.
[2] A. Bhargava, A. Sachdeva, K. Sharma, M. H. Alsharif, P. Uthansakul, and M. Uthansakul, "Hyperspectral imaging and its applications: A review," *Heliyon*, vol. 10, no. 12, Jun. 2024, Art. no. e33208.
[3] C.-I. Chang, *Hyperspectral Data Processing: Algorithm Design and Analysis*. Hoboken, NJ, USA: Wiley, 2013.

[4] N. Dobigeon, Y. Altmann, N. Brun, and S. Moussaoui, "Chapter 6—Linear and nonlinear unmixing in hyperspectral imaging," in *Resolving Spectral Mixtures* (Data Handling in Science and Technology), vol. 30, C. Ruckebusch, Ed., Amsterdam, The Netherlands: Elsevier, 2016, pp. 185–224.

[5] J. Wei and X. Wang, "An overview on linear unmixing of hyperspectral data," *Math. Problems Eng.*, vol. 2020, no. 1, Aug. 2020, Art. no. 3735403.

[6] R. Heylen, M. Parente, and P. Gader, "A review of nonlinear hyperspectral unmixing methods," *IEEE J. Sel. Topics Appl. Earth Observ. Remote Sens.*, vol. 7, no. 6, pp. 1844–1868, Jun. 2014.

[7] N. Dobigeon, J.-Y. Tourneret, C. Richard, J. C. M. Bermudez, S. McLaughlin, and A. O. Hero, "Nonlinear unmixing of hyperspectral images: Models and algorithms," *IEEE Signal Process. Mag.*, vol. 31, no. 1, pp. 82–94, Jan. 2014.

[8] A. Halimi, Y. Altmann, N. Dobigeon, and J.-Y. Tourneret, "Nonlinear unmixing of hyperspectral images using a generalized bilinear model," *IEEE Trans. Geosci. Remote Sens.*, vol. 49, no. 11, pp. 4153–4162, Nov. 2011.

[9] Y. Altmann, A. Halimi, N. Dobigeon, and J.-Y. Tourneret, "Supervised nonlinear spectral unmixing using a postnonlinear mixing model for hyperspectral imagery," *IEEE Trans. Image Process.*, vol. 21, no. 6, pp. 3017–3025, Jun. 2012.

[10] R. Heylen and P. Scheunders, "A multilinear mixing model for nonlinear spectral unmixing," *IEEE Trans. Geosci. Remote Sens.*, vol. 54, no. 1, pp. 240–251, Jan. 2016.

[11] A. Signoroni, M. Savardi, A. Baronio, and S. Benini, "Deep learning meets hyperspectral image analysis: A multidisciplinary review," *J. Imag.*, vol. 5, no. 5, p. 52, May 2019.

[12] J. Chen, M. Zhao, X. Wang, C. Richard, and S. Rahardja, "Integration of physics-based and data-driven models for hyperspectral image unmixing: A summary of current methods," *IEEE Signal Process. Mag.*, vol. 40, no. 2, pp. 61–74, Mar. 2023.

[13] C. Quintano, A. Fernandez-Manso, Y. E. Shimabukuro, and G. Pereira, "Spectral unmixing," *Int. J. Remote Sens.*, vol. 33, no. 17, pp. 5307–5340, 2012.

[14] J. Sigurdsson, M. O. Ulfarsson, and J. R. Sveinsson, "Semi-supervised hyperspectral unmixing," in *Proc. IEEE Geosci. Remote Sens. Symp.*, Jul. 2014, pp. 3458–3461.

[15] N. Dobigeon, J.-Y. Tourneret, and C.-I. Chang, "Semi-supervised linear spectral unmixing using a hierarchical Bayesian model for hyperspectral imagery," *IEEE Trans. Signal Process.*, vol. 56, no. 7, pp. 2684–2695, Jul. 2008.

[16] H. K. Aggarwal and A. Majumdar, "Hyperspectral unmixing in the presence of mixed noise using joint-sparsity and total variation," *IEEE J. Sel. Topics Appl. Earth Observ. Remote Sens.*, vol. 9, no. 9, pp. 4257–4266, Sep. 2016.

[17] T. Ince and T. Dundar, "Simultaneous nonconvex denoising and unmixing for hyperspectral imaging," *IEEE Access*, vol. 7, pp. 124426–124440, 2019.

[18] T. Ince and N. Dobigeon, "Fast hyperspectral unmixing using a multiscale sparse regularization," *IEEE Geosci. Remote Sens. Lett.*, vol. 19, pp. 1–5, 2022.

[19] K. Naganuma and S. Ono, "Toward robust hyperspectral unmixing: Mixed noise modeling and image-domain regularization," *IEEE J. Sel. Topics Appl. Earth Observ. Remote Sens.*, vol. 17, pp. 8117–8138, 2024.

[20] X.-R. Feng, H.-C. Li, R. Wang, Q. Du, X. Jia, and A. Plaza, "Hyperspectral unmixing based on nonnegative matrix factorization: A comprehensive review," *IEEE J. Sel. Topics Appl. Earth Observ. Remote Sens.*, vol. 15, pp. 4414–4436, 2022.

[21] L. Zhuang, C.-H. Lin, M. A. T. Figueiredo, and J. M. Bioucas-Dias, "Regularization parameter selection in minimum volume hyperspectral unmixing," *IEEE Trans. Geosci. Remote Sens.*, vol. 57, no. 12, pp. 9858–9877, Dec. 2019.

[22] D. U. Campos-Delgado, O. Gutierrez-Navarro, J. J. Rico-Jimenez, E. Duran-Sierra, H. Fabelo, S. Ortega, G. Callicó, and J. A. Jo, "Extended blind end-member and abundance extraction for biomedical imaging applications," *IEEE Access*, vol. 7, pp. 178539–178552, 2019.

[23] J. Qin, H. Lee, J. T. Chi, L. Drumetz, J. Chanussot, Y. Lou, and A. L. Bertozzi, "Blind hyperspectral unmixing based on graph total variation regularization," *IEEE Trans. Geosci. Remote Sens.*, vol. 59, no. 4, pp. 3338–3351, Apr. 2021.

[24] J. Yao, D. Hong, L. Xu, D. Meng, J. Chanussot, and Z. Xu, "Sparsity-enhanced convolutional decomposition: A novel tensor-based paradigm for blind hyperspectral unmixing," *IEEE Trans. Geosci. Remote Sens.*, vol. 60, 2022, Art. no. 5505014.

[25] S. Das, A. Routray, and A. K. Deb, "Fast semi-supervised unmixing of hyperspectral image by mutual coherence reduction and recursive PCA," *Remote Sens.*, vol. 10, no. 7, p. 1106, Jul. 2018.

[26] X. Tan, Q. Yu, Z. Wang, and J. Zhu, "Semi-supervised unmixing of hyperspectral data via spectral–spatial factorization," *IEEE Sensors J.*, vol. 21, no. 22, pp. 25963–25972, Nov. 2021.

[27] B. Rasti, A. Zouaoui, J. Mairal, and J. Chanussot, "Fast semisupervised unmixing using nonconvex optimization," *IEEE Trans. Geosci. Remote Sens.*, vol. 62, 2024, Art. no. 5526713.

[28] Q. Wei, M. Chen, J.-Y. Tourneret, and S. Godsill, "Unsupervised nonlinear spectral unmixing based on a multilinear mixing model," *IEEE Trans. Geosci. Remote Sens.*, vol. 55, no. 8, pp. 4534–4544, Aug. 2017.

[29] M. Li, F. Zhu, A. J. X. Guo, and J. Chen, "A graph regularized multilinear mixing model for nonlinear hyperspectral unmixing," *Remote Sens.*, vol. 11, no. 19, p. 2188, Sep. 2019.

[30] M. Li, F. Zhu, and A. J. X. Guo, "A robust multilinear mixing model with $\ell_{2,1}$ norm for unmixing hyperspectral images," in *Proc. IEEE Int. Conf. Vis. Commun. Image Process. (VCIP)*, Dec. 2020, pp. 193–196.

[31] D. U. Campos-Delgado, I. A. Cruz-Guerrero, J. N. Mendoza-Chavarría, A. R. Mejía-Rodríguez, S. Ortega, H. Fabelo, and G. M. Callico, "Nonlinear extended blind end-member and abundance extraction for hyperspectral images," *Signal Process.*, vol. 201, Dec. 2022, Art. no. 108718.

[32] B. Rasti, P. Scheunders, P. Ghamisi, G. Licciardi, and J. Chanussot, "Noise reduction in hyperspectral imagery: Overview and application," *Remote Sens.*, vol. 10, no. 3, p. 482, Mar. 2018.

[33] S. Boyd, "Distributed optimization and statistical learning via the alternating direction method of multipliers," *Found. Trends Mach. Learn.*, vol. 3, no. 1, pp. 1–122, 2010.

[34] J. M. P. Nascimento and J. M. B. Dias, "Vertex component analysis: A fast algorithm to unmix hyperspectral data," *IEEE Trans. Geosci. Remote Sens.*, vol. 43, no. 4, pp. 898–910, Apr. 2005.

[35] M. E. Winter, "N-FINDR: An algorithm for fast autonomous spectral end-member determination in hyperspectral data," *Proc. SPIE*, vol. 3753, pp. 266–275, Jul. 1999.

[36] The MathWorks. (2024). *Parallel Computing Toolbox*. [Online]. Available: https://es.mathworks.com/products/parallel-computing.html

[37] S. Jacques and S. Prahl. *Oregon Medical Laser Center/Assorted Spectra*. Accessed: Sep. 5, 2024. [Online]. Available: https://omlc.org/spectra/index.html

[38] Grupo de Inteligencia Computacional—Universidad del País Vasco/Euskal Herriko Unibertsitatea (UPV/EHU)—Spain. *Hyperspectral Imagery Synthesis (EIAs) Toolbox*. Accessed: Jun. 26, 2024. [Online]. Available: http://www.ehu.es/ccwintco/index.php/Hyperspectral_Imagery_Synthesis_tools_for_MATLAB

[39] S. Ortega, M. Halicek, H. Fabelo, R. Guerra, C. López, M. Lejeune, F. Godtliebsen, G. M. Callicó, and B. Fei, "Hyperspectral imaging and deep learning for the detection of breast cancer cells in digitized histological images," *Proc. SPIE*, vol. 11320, Mar. 2020, Art. no. 113200V.

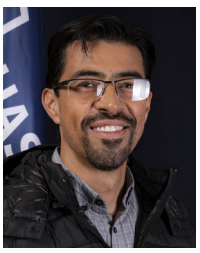

**DANIEL ULISES CAMPOS-DELGADO** (Senior Member, IEEE) received the B.S. degree in electronics engineering from the Autonomous University of San Luis Potosi (UASLP), Mexico, in 1996, and the M.S.E.E. and Ph.D. degrees in electrical engineering from Louisiana State University (LSU), USA, in 1999 and 2001, respectively. In 2001, he joined the School of Science, UASLP, as a Professor. He has published more than 90 peer-reviewed articles in scientific journals and more than 110 in international congresses. His research interests include estimation and detection, optimization algorithms, fault diagnosis, artificial intelligence, and image and signal processing. In these areas, he has received international funding for collaborative work with the University of California, Santa Barbara, Texas A&M University, Institute of Molecular Bioimaging and Physiology, Milan, and the Universidad de Las Palmas de Gran Canaria, Spain. From May 2019 to September 2022, he was an Associate Editor of IEEE Latin America Transactions (LATAMT) (ISSN: 1548-0992), and since January/2024, he has been the Editor-in-Chief of IEEE LATAMT.

**JUAN NICOLÁS MENDOZA-CHAVARRÍA** received the B.S. degree in biomedical engineering and the M.S. degree in electronics engineering from the Universidad Autónoma de San Luis Potosi (UASLP), Mexico, in 2019 and 2022, respectively, where he is currently pursuing the Ph.D. degree in engineering sciences. His research interest includes the use of hyperspectral imaging with IA for medical applications.

**OMAR GUTIERREZ-NAVARRO** (Member, IEEE) received the Bachelor of Science degree in electronics engineering from the Universidad Autónoma de San Luis Potosi (UASLP), San Luis Potosi, Mexico, in 2007, the Master of Science degree in computer science and industrial mathematics from the Centro de Investigación en Matemáticas, Guanajuato, Mexico, in 2010, and the Ph.D. degree in electronics engineering from UASLP, in 2015, concentrating on numerical methods for characterizing in-vivo tissue through time-resolved fluorescence lifetime imaging microscopy data. In 2012, he was awarded the Fulbright-Garcia Robles grant, facilitating his research as a Visiting Scholar with the Biomedical Engineering Department, Texas A&M University, College Station, TX, USA. In 2015, he joined the Biomedical Engineering Department, Universidad Autónoma de Aguascalientes, as a Professor. His research interests include signal processing, machine learning, and multi/hyperspectral imaging applications within food science and biomedical engineering.

**LAURA QUINTANA-QUINTANA** received the bachelor's degree in biomedical engineering from the University Carlos III of Madrid, Spain, in June 2019, and the master's degree in applied electronics and telecommunications from the University of Las Palmas de Gran Canaria, Spain, in 2020. Since then, she has been conducting her research activity with the Integrated Systems Design Division, Research Institute for Applied Microelectronics, University of Las Palmas de Gran Canaria, in the field of bioengineering.

**RAQUEL LEON** received the Telecommunication Engineering, master's, and Ph.D. degrees in telecommunication technologies from ULPGC, Spain, in 2017, 2018, and 2024, respectively. Since then, she has been conducting research with the Integrated System Design Division, Institute for Applied Microelectronics (IUMA), ULPGC, in the field of electronics and bioengineering. In 2020, she obtained a predoctoral research grant from Canary Islands Government. In 2024, she was the Project Manager and a Researcher of the STRATUM European Project. Her current research interest includes the use of hyperspectral imaging for real-time cancer detection.

**SAMUEL ORTEGA** received the B.S.S. degree in telecommunication engineering and the M.Sc. and Ph.D. degrees in telecommunication technologies from the Universidad de Las Palmas de Gran Canaria, Spain, in 2015, 2016, and 2021, respectively. In 2021, he was a Researcher with Norwegian Institute of Food, Fisheries and Aquaculture Research. His research interests include the use of hyperspectral imaging for medical and food quality applications.

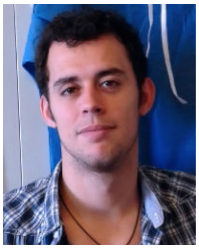

**HIMAR FABELO** received the master's degree in telecommunication engineering and the Ph.D. degree in telecommunication technologies from the Universidad de Las Palmas de Gran Canaria (ULPGC), Spain, in 2014 and 2019, respectively. He has conducted his research activity with the Institute for Applied Microelectronics, ULPGC. In 2022, he obtained the Juan de La Cierva Formación postdoctoral grant at the Fundación Canaria Instituto de Investigación Sanitaria de Canarias (FIISC). He currently works in the STRATUM EU Project, as an Assistant Coordinator and a PI at FIISC. He has published more than 50 journal papers and 60 international conference papers in the field of medical technology, particularly in the application of artificial intelligence and hyperspectral imaging for cancer diagnosis in various medical applications.

**CARLOS LÓPEZ** received the B.Sc. degree in biology from the University Autonoma of Barcelona, in 2001, and the Ph.D. degree with European Mention from University Rovira i Virgili, in 2010. He is the Co-Leader of the Oncological Pathology and Bioinformatics (PO&B) Research Group, Hospital de Tortosa Verge de la Cinta. He has participated in 24 national and international research projects and he has participated in more than 50 national and international conferences with oral communications and scientific posters, and he is the co-author of five book chapters and participated in 51 indexed scientific publications in JCR. His current research interests include digital pathology, artificial intelligence, and the study of immune response in breast cancer patients.

**MARYLÈNE LEJEUNE** received the B.Sc. degree in medical biology and the Ph.D. degree from the Free University of Brussels, in 1990 and 1995, respectively. She has held several fellowships at the Hematology-Oncology Department of "Saint-Pierre," University Hospital Brussels, Belgium, from 1995 to 1998, the Immunology Department, Hospital Clínic of Barcelona, Spain, from 1999 to 2002; and the Anatomy Pathology Department, Verge de la Cinta Hospital of Tortosa (HTVC), Spain, from 2003 to 2009. She has been the Co-Leader of the Oncological Pathology and Bioinformatics (PO&B) Research Group, Pere Virgili Health Research Institute (IISPV), HTVC, since 2009. The group has two complementary lines of research that could lead to the discovery of new biomarkers present in the tumor microenvironment involved in the development of breast cancer and lymphomas. She has been the coordinator of the molecular biology and research area of HTVC, since 2006, and HTVC–IISPV node Biobank, since 2013, and the Technical Manager of the Histological, Cytological and Digitization, IISPV. During all these years, she has participated in 27 scientific research projects (national and European), has conducted and participated in the publication of more than 80 articles in journals included in the Science Citation Index (SCI), has published as first author or co-authored of six book chapters, and has participated in more than 100 communications to national and international congresses.

**GUSTAVO M. CALLICO** (Senior Member, IEEE) received the M.S. degree in telecommunications engineering and the Ph.D. and European Doctorate degrees from the University of Las Palmas de Gran Canaria, in 1995 and 2003, respectively. Since 2022, he has been a Full Professor with ULPGC and develops his research activities with the Institute of Applied Microelectronics (IUMA). He is the co-author of eight book chapters and the author or co-author of more than 230 papers (90 JCR papers) and contributions to technical conferences (140 conferences). He has participated in 27 competitive research projects (6 as PI) and holds two international patents. His current research include hyperspectral systems for cancer detection, artificial intelligence algorithms, real-time superresolution algorithms, synthesis-based design for SOCs, and circuits for multimedia processing and video coding standards. He was a Senior Associate Editor of IEEE TRANSACTIONS ON CONSUMER ELECTRONICS from 2008 to 2022 and has been an Associate Editor of IEEE ACCESS since 2016 and *Microprocessors and Microsystems* (Elsevier) since 2022.